

# IDEA League



MASTER OF SCIENCE IN APPLIED GEOPHYSICS  
RESEARCH THESIS

---

## Investigating S-wave Anisotropy in the Rotondo Granite by Crosshole Seismic Surveys

María Blanch Jover

---

August 4, 2023



# Investigating S-wave Anisotropy in the Rotondo Granite by Crosshole Seismic Surveys

MASTER OF SCIENCE THESIS

for the degree of Master of Science in Applied Geophysics at  
ETH Zürich  
by

María Blanch Jover

August 4, 2023



IDEA LEAGUE  
JOINT MASTER'S IN APPLIED GEOPHYSICS

Delft University of Technology, The Netherlands  
ETH Zürich, Switzerland  
RWTH Aachen, Germany

Dated: *August 17, 2023*

Supervisors:

---

Marian Hertrich

---

Kathrin Behnen

Committee Members:

---

Marian Hertrich

---

Kathrin Behnen

---

Florian Wagner



---

# Abstract

The Bedretto Laboratory, located within the Rotondo granite, conducts stimulations of the host rock to investigate the possibility of enhanced geothermal energy and tries to better understand the risk of induced seismicity. Seismic anisotropy plays an important role when processing seismic data, making its characterization essential in such a laboratory. In a previous study, through crosshole seismic, the apparent velocity of P-waves was obtained and used to give some first values of the parameters characterising anisotropy assuming a Tilted Transversely Isotropic medium (TTI). Further investigating the obtained data, S-wave splitting could be detected. This phenomenon occurs in anisotropic media, resulting in horizontal S-waves (SH) and vertical S-waves (SV) having different seismic velocities. A sensitivity analysis was performed to assess the significance of S-wave information. The analysis revealed the benefit of incorporating the information provided by the S-waves to improve the current anisotropic model. Several crosshole surveys were carried out using different instruments, such as a S-wave sparker or a 3-component geophone. The aim was to understand the behavior of S-waves better and accurately identify the arrival time of both types of waves. The results reveal that rotating the 3-component geophones data was the best choice to isolate both types of S-waves. Time arrivals were picked, and apparent velocities were calculated knowing the ray path length. They show a change from 2747 m/s to 3216m/s for SH waves, and from 2830m/s to 3105m/s for SV-waves. An attempt was made to obtain the anisotropy parameters that successfully describe the observed velocities in the Rotondo granite.



---

# Acknowledgements

First, I would like to thank Dr. Marian Hertrich and Kathrin Behnen for all their support and help throughout this study. I appreciate the interesting discussions that we have shared about anisotropy and inverse theory, they made me better understand the topic and kept me motivated. I sincerely value their guidance and encouragement during the project. I am also thankful for everyone that helped with the data acquisition in Bedretto. A special thanks goes to the entire Bedretto Team for all the support provided during my stays there and for creating such an enjoyable working environment. I am also grateful to Dr. Maurer Hansruedi for his time listening to my project and providing valuable insight into the sensitivity analysis part. I thank Dr. David Sollberger for providing scripts for three component simulations. I would like to acknowledge also my office mates and roommates for hearing my concern, for cheering for me when needed, and for their company during this time. Last but not least, I would also like to thank my family and friends for loving and supporting me during this master's.

ETH Swiss Federal Institute of Technology  
August 4, 2023

María Blanch Jover



---

# Table of Contents

<b>Abstract</b>	<b>v</b>
<b>Acknowledgements</b>	<b>vii</b>
<b>Nomenclature</b>	<b>xv</b>
<b>Acronyms</b>	<b>xv</b>
<b>1 Introduction</b>	<b>1</b>
<b>2 Site Description</b>	<b>3</b>
2-1 Bedretto Lab and Geology of the Region . . . . .	3
2-1-1 Stress Conditions . . . . .	4
2-1-2 Borehole Characteristics . . . . .	4
<b>3 Anisotropy</b>	<b>7</b>
3-1 Wave Equation and Hook's Law . . . . .	7
3-2 Seismic Anisotropy . . . . .	8
3-2-1 Transverse Tilted Anisotropy . . . . .	11
<b>4 Stereonet Representation</b>	<b>13</b>
4-1 Coordinate Convention . . . . .	14
<b>5 Inverse Theory</b>	<b>15</b>
5-1 Linear Inverse Problems . . . . .	15
5-1-1 Least-Squares Method . . . . .	16
Predicted error . . . . .	16
Damping constraints . . . . .	17
Smoothing . . . . .	17
5-2 Non-linear inverse problems . . . . .	17
Data resolution matrix . . . . .	19

<b>6</b>	<b>Motivation</b>	<b>21</b>
6-1	P-wave Crosshole Seismic . . . . .	21
6-1-1	Detection of S-wave Splitting . . . . .	22
6-2	Sensitivity Analysis . . . . .	23
	Data resolution matrix . . . . .	27
<b>7</b>	<b>S-wave Characterization</b>	<b>31</b>
7-1	S-wave Sparker . . . . .	31
7-1-1	Data Processing . . . . .	31
7-1-2	Results . . . . .	32
7-2	3-Component Geophone . . . . .	34
7-2-1	Hammering Test . . . . .	34
7-2-2	Crosshole Seismics . . . . .	35
	Raw data . . . . .	35
	Data rotation . . . . .	37
7-3	Full 3-component Geophone Survey . . . . .	37
7-3-1	Data Processing . . . . .	39
7-3-2	Rotation . . . . .	39
7-3-3	Picking . . . . .	40
<b>8</b>	<b>Results</b>	<b>43</b>
8-1	Apparent Velocities . . . . .	43
8-2	Inversion . . . . .	44
<b>9</b>	<b>Conclusion</b>	<b>47</b>
	<b>Bibliography</b>	<b>49</b>
<b>A</b>	<b>Appendix 1</b>	<b>51</b>
A-1	Crosshole seismic with S-wave sparker . . . . .	51
A-2	3-component geophone . . . . .	53
A-2-1	Hammering test . . . . .	53
A-2-2	Crosshole seismic . . . . .	53
A-2-3	Full 3-component geophone survey . . . . .	56

---

# List of Figures

2-1	a) Map view of the location of the Bedretto Tunnel and of the Rottondo granite. b) Cross-sectional view of the tunnel with the location of the Bedretto Lab. Figure from Ma et al. (2021). . . . .	4
2-2	Relative position of the three Short Boreholes in which this project will focus on.	5
3-1	Schematic sketch of a) a VTI medium; b) a TTI medium, from Fa et al. (2020).	9
4-1	Visualization of how different rays lay in the stereonet representation. . . . .	13
6-1	Shot gather recorded from SB2.3 and shot from SB2.2 at a 16m depth along the borehole. The expected arrival time for the different wave types has been superimposed. . . . .	23
6-2	Distance, dip and azimuth of the ray of the survey conducted by Epiney (2022) and used for the sensitivity analysis. . . . .	24
6-3	Left: Jacobian matrix. Right: Jacobian matrix using a logarithmic scale. . . . .	24
6-4	Sensitivities of the different model parameters for P-waves plotted in a stereonet.	26
6-5	Sensitivities of the different model parameters for SV-waves plotted in a stereonet	26
6-6	Sensitivities of the different model parameters for SH-waves plotted in a stereonet	26
6-7	Data resolution matrix. . . . .	28
6-8	Importance of the data resolution matrix plotted in the stereonet. . . . .	29
7-1	Shot gather using the S-wave sparker for the 7 different rotations of the instrument around its own. The source was placed at a depth of SB2.3 at 38 m, and the receiver was at 24 m in SB2.2. . . . .	33
7-2	Receiver gather when the 3-component geophone was placed in SB2.3 using a hammer as a source. . . . .	34
7-3	Receiver gather of raw crosshole seismic data using a 3-component geophone. The upper image corresponds to a receiver depth of 10 m while the second one corresponds to 24.8 m. . . . .	36

7-4	Receiver gather of the stacked and rotated seismic data. The upper image corresponds to a receiver depth of 10 m while the second corresponds to 24.8 m. . . . .	38
7-5	Receiver gather with the 3-component geophone placed at 22 m depth in borehole SB2.2 and shots were made at SB2.3. . . . .	39
7-6	Receiver gather after being rotated where the 3-component geophone was placed at 22 m depth in borehole SB2.2 and shots were made at SB2.3. . . . .	40
7-7	Receiver gather with the travel times picked for when the receiver was placed at 29 m depth in borehole SB2.2 and shots were made at SB2.3. . . . .	41
8-1	Velocities measured from the picked times arrivals. . . . .	43
8-2	Predicted velocities using the model parameters in table 6-2 . . . . .	44
8-3	Velocity distribution using the model parameters obtained after optimization. . . . .	45
8-4	Difference between the apparent velocities and the obtained with the optimized model parameters. . . . .	46
8-5	Histogram of the residual for the initial model parameters and for the obtained ones from the optimization procedure. . . . .	46
A-1	Shot gather using S-waves sparker. Left: raw data. Right: filtered data with a highpass filter for 60 Hz. . . . .	51
A-2	Cable orientation at the top of the borehole for each rotation step. . . . .	52
A-3	Scheme of the rays for the survey conducted on April 27. The 3-component geophone was at SB2.3 and the tunnel floor was hammered with 1 m spacing. . . . .	53
A-4	Receiver gather when the 3-component geophone was placed in SB2.3 using a hammer as a source when the right side of the rail was being hammered. . . . .	54
A-5	Receiver gather when the 3-component geophone was placed in SB2.3 using a hammer as a source when the left side of the rail was being hammered. . . . .	54
A-6	Ray path representation for the cross-hole survey where the 3 component geophone was positioned at two different depths in SB2.3 and the source position was varied at SB2.1. . . . .	55
A-7	Receiver gather after being rotated where the 3-component geophone was placed at 36 m depth in borehole SB2.2 and shots were made at SB2.3. It can be seen that no signal is recorded for the y-component of the geophone. . . . .	56

---

# List of Tables

2-1	Borehole properties of the SB of interest. . . . .	4
6-1	Anisotropy parameters for the Rotondo grinite found by Epiney (2022). . . . .	22
6-2	Values of the different parameters needed to do the calculation of the expected arrival time of the different wave types. . . . .	22
7-1	Specifications of the crosshole seismic carried using the 3 component geophone. . . . .	35
8-1	Values found for the model parameters after the optimization procedure. . . . .	45



---

# Acronyms

**ETH** Swiss Federal Institute of Technology

**VTI** Vertical Transverse Isotropy

**TTI** Tilted Transverse Isotropy

**BULGG** Bedretto Underground Laboratory for Geosciences and Geoenergies

**SB** Stress Boreholes

**TM** Tunnel Meter

**EGS** Enhanced Geothermal Systems

**LSQR** Least-Squares method



---

# Chapter 1

---

## Introduction

The recent increase in energy consumption, the limited amount of fossil fuels, and the negative impact that these have on the environment have led to an increase in the research for cleaner energy sources (Coskun et al., 2014). Among these, geothermal energy plays a significant role due to its continuous generation of energy and its relatively cheap extraction. Electricity production comes mainly from deep geothermal and can be obtained in two ways: from hydrothermal systems and from Enhanced Geothermal Systems (EGS) (Bauer et al., 2017). For a hydrothermal system, specific conditions are needed such as high underground temperatures ( $<100^{\circ}\text{C}$ ), reservoirs with enough water, or a formation with enough permeability for the extraction. Unfortunately, these conditions are only fulfilled in a few places in the world. However, EGS is independent of the amount of water in the formation but makes use of the temperature gradient in Earth's interior.

EGS involves drilling and connecting two or more wells. Cold water is injected into the formation, which gets heated and later pumped back to the surface (Bauer et al., 2017). This method primarily relies on reaching a significant temperature gradient within the geological formation. EGS also strongly depends on the technical challenges such as drilling, enhancing the permeability in the formation, or the treatment of mineral scaling during operation. To enhance the permeability of the reservoir, hydraulic stimulation is carried (Shakas et al., 2020). This is necessary for reservoirs with crystalline basement rocks where permeability is significantly low.

In situ laboratories have recently become essential for bridging the gap between laboratory-scale experiments and reservoir-scale conditions. Many underground facilities have been constructed from existing mines and tunnels or have been excavated (e.g., Äspö, Canadian URL, Grimsel, Jinping, Kamaishi, KURT, Mont Terri, Reiche Zeche, SURF) (Ma et al., 2021). Among them, the Bedretto Underground Laboratory for Geosciences and Geenergies (BULGG) was established in the Swiss Alps to study the behavior of the deep subsurface by accessing and stimulating it. Stimulation can trigger seismic events, so it is essential to monitor it over time (Shakas et al., 2020). The primary technique for it is through recording the seismic signal.

Most rocks are found to be anisotropic as [Thomsen \(1986\)](#) pointed out. There are differences in wave propagation for an anisotropic media compared to a isotropic one as phase velocity and group velocity are no longer the same. This leads to shear wave splitting resulting in three body wave modes: one quasi-compressional wave (qP) and two quasi-shear waves (qSV and qSH). Each propagates with a different velocity and polarization direction ([Bai et al., 2013](#)). Therefore, it is important to consider this effect to process seismic data properly.

Previous studies in the host rock of the BedrettoLab, have proven the anisotropy of the formation ([Epiney, 2022](#)). A crosshole seismic survey was carried out in 2022 in three of the borehole of the facility. It covered a wide range of azimuths, dips and distances and with travel times along straight rays, and by picking the apparent velocity for P-waves was obtained. The Thomsen parameters and the inclination and azimuth of the symmetry axis were found with inversion methods. The rock fit satisfactorily to a Tilted Transverse Isotropy (TTI) model.

Within this project's scope, a further understanding of the anisotropy in the BedrettoLab host rock is aimed. In this case, the study focuses on the information provided by S-waves splitting, also known as bi-refringence. A characteristic of the splitting is that the polarization of the leading split shear waves is usually parallel to the direction of maximum compressional stress ([Holmes et al., 1993](#)). We aim to detect the splitting in the Bedreto granite in in-situ conditions. To achieve this goal, we do a sensitivity analysis to asses the significance that S-waves information provides. This is done to determine if the incorporation of S-waves data will improve the anisotropy parameters found by [Epiney \(2022\)](#) for a TTI medium. Different methods to obtain S-waves information are explored and the most effective one is found to be the utilization of a 3-component geophone. From the data acquired with it, we find apparent velocities from travel time arrivals that we manually pick of the wave. Finally, we attempt to perform an inversion in order to obtain new anisotropy parameters that better explain the behavior of the three waves.

---

## Chapter 2

---

# Site Description

This chapter will present an overview of the site where this project has been carried out. The main reason for the existence of this laboratory will be explained, as well as its most relevant geological characteristics. In addition, in section (2-1-2), the specific characteristics of the boreholes used for this study will be detailed.

### 2-1 Bedretto Lab and Geology of the Region

The ~5 km long Bedretto tunnel connects the Fruka Base Tunnel with the Bedretto Valley (Ticino, Switzerland). The tunnel was constructed between 1971 to 1982 as part of the logistics of the Furka Base Tunnel to transport the muck. Currently, the tunnel hosts the Bedretto Underground Laboratory for Geosciences and Geoenergies (BULGG), operated by the Swiss Federal Institute of Technology (ETH) since 2019 (Rast et al., 2022). In it, techniques for extracting geothermal energy in low permeability systems are tested as well as research on seismicity and earthquake detection.

The south portal of the tunnel has an elevation of 1479.5 meters above sea level (m.a.s.l.) and the junction with the Furka Base Tunnel is 1505.2 m.a.s.l., which leads to a mean slope of 0.5% along the tunnel. The Tunnel Meter (TM) system is usually used to determine the distances, with 0 TM at the southern entrance. The laboratory is located between 2000 and 2100 TM, in a zone where the tunnel widens to 6 m. The overburden increases progressively along the tunnel, reaching 1000 m in the laboratory and having its maximum of 1632 m at 3140 MT. The tunnel encounters subvertically dipping fractures and fault zones. The predominant strike is SW-NE to WSW-ESE (Lützenkirchen and Loew, 2011) and they are mostly dipping more than 50°.

The Bedretto tunnel crosses three geological units of the Gotthard massif (Rast et al., 2022): the Tremola series (0-434 TM), the Prato series (434-1138 TM), and the Rotondo granite (1138-5218 TM). The latter one is the host of the laboratory. The Rotondo granite is a magmatic body whose intrusion took place around  $294 \pm 1.1$  Ma in the late-Variscan (Sergeev et al., 1995). This is mostly equigranular and fine-grained granite. Upon visual inspection

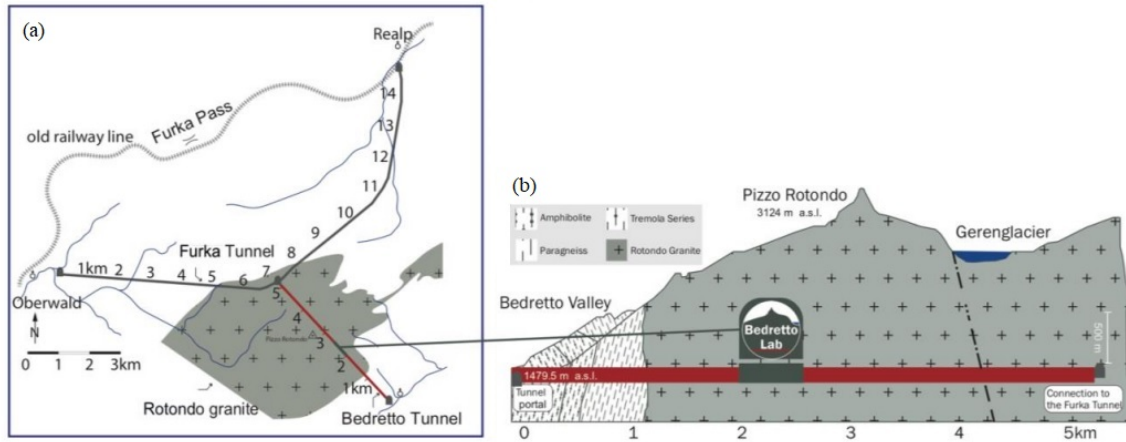


**Figure 2-1:** a) Map view of the location of the Bedretto Tunnel and of the Rotondo granite. b) Cross-sectional view of the tunnel with the location of the Bedretto Lab. Figure from Ma et al. (2021).

of the granite exposed on the tunnel walls, it appears homogeneous and isotropic. However, recent studies indicate that the Rotondo granite exhibit moderate seismic anisotropy (David et al., 2020).

### 2-1-1 Stress Conditions

Six Stress Boreholes (SB) were drilled to carry out a hydraulic fracturing test that was conducted between December 2018 and July 2019. Each SB has a depth of 30-40 m and is strategically positioned to avoid major fault zones. An in situ stress field estimation was obtained from the hydraulic fracturing test (Bröker and Ma, 2022). The average direction of the maximum horizontal stress is N100-110°E. The estimation of the minimum ( $S_{hmin}$ ) and maximum stress ( $S_{Hmax}$ ) are respectively  $14.6 \pm 1.4$  MPa and  $24.6 \pm 2.6$  MPa. The overburden stress is  $\sim 26.5$  MPa, obtained from integrating the density along the overburden. Therefore this leads to the following relation:  $S_v \geq S_{Hmax} > S_{hmin}$ . During the same test, the pore pressure was also measured, ranging between 2 and 5.6 MPa, and generally increasing with depth.

### 2-1-2 Borehole Characteristics

Borehole	Position (TM)	Depth (m)	Azimuth (deg)	Inclination (deg)	Diameter (mm)
SB2.1	2066	29.9	38.8	89.8	101
SB2.2	2075	40	226.9	60	101
SB2.3	2095	39.9	133.9	70	101

**Table 2-1:** Borehole properties of the SB of interest.

In this project, we focused on three of the SB drilled in the first stages of the BULGG: SB2.1, SB2.2 and SB2.3. They are located in the lab niche short distances from each other. The relative position in the tunnel can be seen in figure (2-2) and their specific characteristics can be seen in table (2-1). It can be noticed that the axis of the boreholes is not parallel to each other, but they have a certain relative inclination. This leads to a wide range of distances, azimuths and dips of the rays when conducting crosshole surveys. The minimum distance between the possible source and receiver setups is 8.9 m and the maximum goes up to 45.4 m.

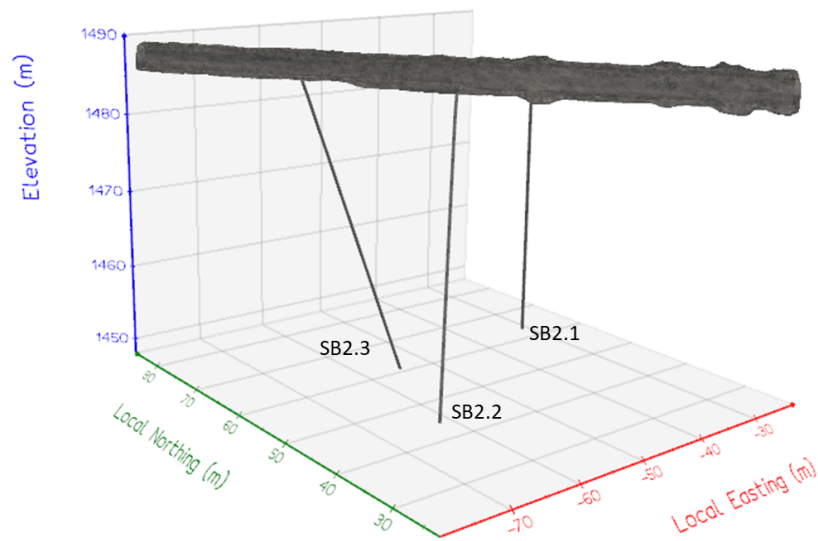


**Figure 2-2:** Relative position of the three Short Boreholes in which this project will focus on.



---

## Chapter 3

---

# Anisotropy

In the following chapter, we derive the equations governing seismic anisotropy and explore their implications for this type of medium. For that, we introduce the wave equation and we present particular cases for different approximations of the stiffness tensors.

### 3-1 Wave Equation and Hook's Law

From the second law of Newton, when applied to a certain volume within a continuum, the general wave equation can be obtained. This can be expressed as:

$$\rho \frac{\partial^2 u_i}{\partial t^2} - \frac{\partial \sigma_{ij}}{\partial x_j} = f_i \quad (3-1)$$

where  $\rho$  is the density,  $u_i$  is the displacement,  $f_i$  is the source term,  $t$  is time and  $x_{j,i}$  are the Cartesian coordinates. The equation contains two unknowns: the displacement vector and the stress tensor. In the limit of small strain, the generalized Hooke's law establishes a linear relationship between stress and strain:

$$\sigma_{ij} = c_{ijkl} \epsilon_{kl} \quad (3-2)$$

where  $c_{ijkl}$  is a fourth-order tensor of stiffness and  $\epsilon$  is the strain tensor defined as:

$$\epsilon_{ij} = \frac{1}{2} \left( \frac{\partial u_k}{\partial x_l} + \frac{\partial u_l}{\partial x_k} \right) \quad (3-3)$$

Substituting expression (3-3) into (3-2) and this one in (3-1), the equation of motion describing the propagation of waves in rock can be written as:

$$\rho \frac{\partial^2 u_i}{\partial t^2} - \frac{\partial}{\partial x_j} \left( c_{ijkl} \frac{\partial u_k}{\partial x_l} \right) = f_i \quad (3-4)$$

The stiffness tensor has 81 coefficients called elastic constants, measured in Pa. Due to the conservation of angular momentum and energy, it can be seen that the stress and strain tensors are symmetric. This leads to:

$$c_{ijkl} = c_{jikl}; c_{ijkl} = c_{ijlk} \quad (3-5)$$

From thermodynamics considerations, it can also be seen that:

$$c_{ijkl} = c_{klij} \quad (3-6)$$

Applying these symmetries the number of independent coefficients gets reduced to 21.

With the simplification of the coefficients, the fourth order stiffness tensor can be reduced to a 6x6 matrix (Tsvankin, 2012). For that, each pair of indices  $ij$  and  $kl$  is replaced by a single index using Voigt notation,  $\alpha$  and  $\beta$  respectively. Therefore, the substitution scheme results in: 11→1, 22→2, 33→3, 32=23→4, 31=13→5 and 12=21→6. Thus, equation (3-2) can be written as:

$$\sigma_\alpha = c_{\alpha\beta} \epsilon_\beta \quad (3-7)$$

For different types of material symmetries, different components of the elastic modulus are non-zero (Thomsen (1986)). The case with higher symmetry is the isotropic one, where there are only two elastic constants, and the matrix is reduced to:

$$c_{\alpha\beta} = \begin{bmatrix} c_{33} & (c_{33} - 2c_{44}) & (c_{33} - 2c_{44}) & & & \\ (c_{33} - 2c_{44}) & c_{33} & (c_{33} - 2c_{44}) & & & \\ (c_{33} - 2c_{44}) & (c_{33} - 2c_{44}) & c_{33} & & & \\ & & & c_{44} & & \\ & & & & c_{44} & \\ & & & & & c_{44} \end{bmatrix} \quad (3-8)$$

By substituting the matrix in equation (3-8), the wave equation for the isotropic medium can be obtained.

## 3-2 Seismic Anisotropy

Anisotropy is the variation of a property with respect to the direction in which it is measured. Seismic anisotropy refers to the change of velocity at which waves propagate depending on the direction. From now on, whenever we mention anisotropy, we will refer to seismic anisotropy.

Anisotropy can be caused by three main factors (Cerveny, 2001):

1. Inherent anisotropy: this could be due to crystal anisotropy when a crystalline solid has a preferred orientation, or stress-induced anisotropy: an isotropic solid can become anisotropic when significant stresses are applied.
2. Crack-induced anisotropy: inclusions such as cracks, pores, fractures or impurities can cause anisotropy if observed at long wavelengths.
3. Long-wavelength anisotropy: occurs when regular sequences of thin layers are observed with a wavelength longer than their thickness, causing the system to behave anisotropically.



where  $\theta$  is the inclination of the ray and  $D(\theta)$  is:

$$D(\theta) = \{(c_{33} - c_{44})^2 + 2[2(c_{13} - c_{44})^2 - (c_{33} - c_{44})(c_{11} + c_{33} - 2c_{44})] \sin^2 \theta + [(c_{11} + c_{33} - 2c_{44})^2 - 4(c_{13} + c_{44})^2] \sin^4 \theta\}^{\frac{1}{2}} \quad (3-11)$$

Due to the complexity of the equations, [Thomsen \(1986\)](#) introduced three parameters to simplify the expressions. These can be written as:

$$\epsilon = \frac{C_{11} - C_{33}}{2C_{33}} \quad (3-12a)$$

$$\gamma = \frac{C_{66} - C_{44}}{2C_{44}} \quad (3-12b)$$

$$\delta = \frac{(C_{13} + C_{44})^2 - (C_{33} - C_{44})^2}{2C_{33}(C_{33} - C_{44})} \quad (3-12c)$$

Where  $\delta$  is the simplified version after assuming weak anisotropy ( $\ll 1$ ).

These three parameters are dimensionless and they go to zero for the case of an isotropic media. The parameter  $\epsilon$  is the fractional difference between the horizontal and vertical P-wave velocity ([Tsvankin, 2012](#)). A positive value implies that the horizontal P-wave velocity is more significant than the vertical one. Similarly,  $\gamma$  represents the equivalent measure for the case of SH-waves. Laboratory and field data show that the velocity of P and SH-waves in the direction of the symmetry axis is usually lower than in the plane. Therefore,  $\epsilon$  and  $\gamma$  are typically positive. Lastly, the parameter  $\delta$  is the second derivative of the P-wave phase-velocity function at vertical incidence. Thus, P-waves velocity will be higher away from the vertical if  $\delta$  is positive and lower if it is negative ([Tsvankin, 2012](#)).

Using the Thomsen parameters and assuming weak anisotropy, the three solutions of the motion equation can be simplified to:

$$v_P(\theta) = \alpha_o(1 + \delta \sin^2 \theta \cos^2 \theta + \epsilon \sin^4 \theta) \quad (3-13a)$$

$$v_{SV}(\theta) = \beta_o \left[ 1 + \frac{\alpha_o^2}{\beta_o^2} (\epsilon - \delta) \sin^2 \theta \cos^2 \theta \right] \quad (3-13b)$$

$$v_{SH}(\theta) = \beta_o(1 + \gamma \sin^2 \theta) \quad (3-13c)$$

where  $\alpha_o$  and  $\beta_o$  are vertical sound speeds for P and S waves respectively and can be expressed as:

$$\alpha_o = \sqrt{\frac{C_{33}}{\rho}} \quad \text{and} \quad \beta_o = \sqrt{\frac{C_{44}}{\rho}} \quad (3-14)$$

Looking at the equation (3-13) we see that the phase velocity of SH waves is only controlled by the parameter  $\gamma$ . In the case of the P-wave velocity, the parameter that mainly controls this value is  $\delta$  for when near the symmetry axis. Near the isotropy plane, parameter  $\epsilon$  is the dominant one. Another observation that can be made is that, for weak anisotropy, SV-wave phase velocity is symmetric for  $\theta = 45^\circ$ .

It is worth noting that there is no azimuthal dependency for VTI. This is because the medium is symmetric around the vertical axis, and the properties of the medium are the same in all directions that lie in perpendicular planes to the symmetry axis. Therefore, there is only a dependency on the inclination of the ray.

### 3-2-1 Transverse Tilted Anisotropy

When the symmetry axis is rotated by a certain angle with respect to the normal, a **TTI** medium is obtained. In this case, the rotational symmetry for a **VTI** medium is no longer vertical. Thus, there is no longer a dependency only on the dip for the velocity of the seismic waves but also on the azimuth. In this case, two pair of angles are needed to accurately describe the velocity of the different waves that travel in this medium. One pair of dip and azimuth that determine the orientation of the symmetry axis  $(\theta_o, \phi_o)$ , and one that determines the direction of the ray propagation  $(\theta, \phi)$ .

For this type of medium the equations introduced by Thomsen (3-13), are still valid. However, the angle  $\theta$  is no longer directly the dip but is the angle subtended between the arbitrary symmetry axis direction and the slowness vector direction. This angle can be defined as:

$$\nu = \cos(\sin(\theta_o) \sin(\theta) \cos(\phi_o - \phi) + \cos(\theta_o) \cos(\theta))^{-1} \quad (3-15)$$

In this section we also introduce the notation used by Bai et al. (2013) for the case of a **TTI** medium. In this one, parameters P and Q are being used and they can be expressed as:

$$P = (Q_1 + Q_2)/2 \quad (3-16a)$$

$$Q = Q_1 Q_2 - Q_3 \quad (3-16b)$$

Where  $Q_1$ ,  $Q_2$  and  $Q_3$  are defined as:

$$Q_1 = a_{44} + (a_{11} - a_{44}) \sin(\nu)^2 \quad (3-17a)$$

$$Q_2 = a_{33} + (a_{44} - a_{33}) \sin(\nu)^2 \quad (3-17b)$$

$$Q_3 = \frac{1}{4}(a_{13} + a_{44}) \sin(\nu)^2 \quad (3-17c)$$

Where  $a$  is the elastic modulus parameters normalized by the density. With parameters P and Q, we find that the phase velocity for each mode is:

$$v_{P,SV} = \sqrt{P \pm \sqrt{P^2 - Q}} \quad (3-18a)$$

$$v_{SH} = \sqrt{a_{44} + (a_{66} - a_{44}) \sin(\nu)^2} \quad (3-18b)$$

Expanding equations (3-18), we arrive at the same expressions as those derived by Thomsen (1986). Bai et al. (2013) alternative on expressing the phase velocity for the different waves is more convenient when working in programming languages, as it is written concisely. On the other hand, Thomsen equations are written in a way that it is easier to interpret the physical principles underlying the velocities.



## Stereonet Representation

To characterize the anisotropy, the velocity of the different wave types in different directions is necessary. The arrival times of the waves are obtained from the seismic data. We consider that we have a ray from the source to the receiver defined by its azimuth, dip and length, we can calculate the apparent velocities by dividing the distance by the arrival times. To visually represent the relationship between velocity and ray orientation, a stereonet representation has been designed.

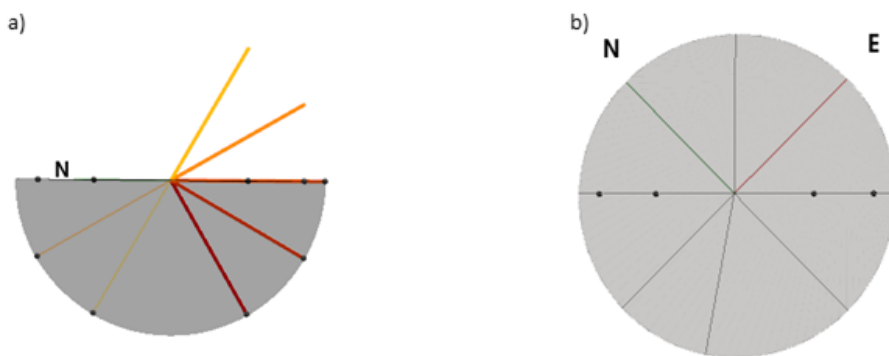


**Figure 4-1:** Visualization of how different rays lay in the stereonet representation.

The process of displaying the rays as points on a stereonet is as follows. First, we omit the ray's length as each can be uniquely characterized by its dip and azimuth. Rays with a negative dip are located in the lower hemisphere, while rays with a positive dip are in the upper one. Each of these rays intersects at a specific point in the unit sphere. We extend the upward-going ones until their intersection with the lower hemisphere. This interception with the lower hemisphere is then projected onto the horizontal plane that is cutting the

sphere's center. Thus, the three-dimensional representation (dip, azimuth and the velocity or the parameter that we want to represent) has been reduced to a point in a two-dimensional representation.

Figure (4-1) shows various examples of the representation of different rays with distinct dips on the stereonet. It can be noticed, that two rays with the same azimuth but opposite dips, their projection on the stereonet is identical. It can also be seen that the plot of rays with the same azimuth but different dip lies in a straight line. Similarly, concentric circles correspond to a constant dip, while rotating around the circle varies the azimuth.

## 4-1 Coordinate Convention

It is known that in the spherical coordinate system, the azimuth varies  $360^\circ$  while the dip is only  $180^\circ$ . There are many ways to express how these two angles vary. Thus, it is necessary to have a clear system to unify their expression. In the case of this project, we have used the system used in Bedretto. In it, the dip goes from  $-90^\circ$  when the ray is vertical pointing upwards to  $90^\circ$  when it pointing downwards. Thus, when the ray is horizontal, the dip is  $0^\circ$ . In the case of the azimuth, it goes from  $0^\circ$  when the ray is pointing North to  $360^\circ$  clockwise. Therefore a  $90^\circ$  azimuth would correspond to the ray pointing east.

---

## Chapter 5

---

# Inverse Theory

Inverse theory is the process of obtaining the properties of a system from observations (Fichtner, 2021). It has three main components: the observed data, the unknown properties we want to obtain, and a physical relationship between them. We can have a linear or non-linear problem depending on the relationship. Considering the equations in chapter (3), we have a non-linear case. However, in this section, we will first introduce the equations for the linear case where it is easier to introduce the fundamental concepts to later generalize for the non-linear one.

### 5-1 Linear Inverse Problems

In a problem where the relationship between data and the physical parameter is linear, it can be written that:

$$d = Gm \quad (5-1)$$

where  $d$  is a column vector of length  $N$  with the response of the system,  $m$  is an  $M$  length column vector with the physical parameters and  $G$  is an  $N \times M$  coefficient matrix that carries the physical relationship between  $d$  and  $m$ .

In our case, the observed data ( $d$ ) are the travel times picked for the different wave types. The parameters that we want to obtain ( $m$ ) are seven: the three Thomsen parameters, the velocities in the direction of the symmetry axis for P and S-waves and the dip and azimuth of the symmetry axis:  $\epsilon$ ,  $\delta$ ,  $\gamma$ ,  $\alpha_o$ ,  $\beta_o$ ,  $\theta_o$  and  $\phi_o$ . Therefore, we have that  $M=7$ . Lastly, the  $G$  matrix that relates  $d$  and  $m$  can be found from equations (3-10). We assume that the rays' dip ( $\theta$ ), the azimuth ( $\phi$ ) and the distance ( $d$ ) are known.

Obtaining the parameters can be done by simply inverting the matrix  $G$ . Thus, it is obtained:

$$m_{est} = G^{-1}d_{obs} \quad (5-2)$$

However, this matrix is not always invertible. This is dependent on the number of data points that we have ( $M$ ) and the number of parameters we want to obtain ( $N$ ) (Yogeshwar, 2022). There are three different cases:

1. Even-determined ( $N = M$ ): same number of data points as parameters. The matrix  $G$  is squared and can be inverted.
2. Over-determined ( $N > M$ ): more data points than parameters. There is no exact solution of equation (5-1), the problem is solved using Least-Squares method (LSQR) which gives the best approximation.
3. Under-determined ( $N < M$ ): less data points than parameters. There are infinite solutions, additional information is needed and the problem is solved using Minimum-Length solution.

In our case, it is usual to have more data points than parameters to determine, we have an over-determined system. Therefore, from now on, we will only focus on the derivation of the solution of the inverse problem for this specific case.

### 5-1-1 Least-Squares Method

The Least-Squares method (LSQR) solution is obtained by trying to find the one that is the closest to the observations (Yogeshwar, 2022). Thus, the aim is to minimize the difference between the predicted and obtained data. With this purpose, an objective function ( $\phi$ ) is formulated:

$$\phi(m) = e^T e = (d_{obs} - d_{pred})^T (d_{obs} - d_{pred}) = (d_{obs} - Gm)^T (d_{obs} - Gm) \quad (5-3)$$

Which can be minimized by:

$$\frac{\partial \phi}{\partial m} = 0 \quad (5-4)$$

And solving, the LSQR solution is obtained as:

$$m_{est} = [G^T G]^{-1} G^T d_{obs} \quad (5-5)$$

Where we assume that  $[G^T G]$  is invertible. To simplify the notation, we will refer to  $[G^T G]^{-1} G^T$  as  $G^{-g}$  from now on. Thus, it follows that the solution to our inverse problem is simplified as:

$$m_{est} = G^{-g} d_{obs} \quad (5-6)$$

Having obtained the vector with the predicted physical parameters  $m$ , the data can be estimated as:

$$d_{pred} = Gm_{est} \quad (5-7)$$

### Predicted error

In the previous section, we have not considered the errors of the observed data points. They can affect the quality of the least-squares solution. The error can be used as a data weighting factor (Yogeshwar, 2022). The data points with a higher error (less accurate) should be taken less into consideration, and therefore have a smaller weight in the solution of the LSQR than the ones with high accuracy.

The weighting matrix can be written as:

$$W_d = \begin{pmatrix} \frac{1}{\epsilon_1} & & & & & \\ & \frac{1}{\epsilon_2} & & & & \\ & & \ddots & & & \\ & & & \frac{1}{\epsilon_{N-1}} & & \\ & & & & \frac{1}{\epsilon_N} & \end{pmatrix} \quad (5-8)$$

Where  $\epsilon_i$  is the error for each data point. The same error can be used in the case of not having different error values for each data point. The forward problem can be rewritten as:

$$W_d d = W_d G m \quad (5-9)$$

### Damping constraints

When we have prior knowledge of what a parameter value is supposed to be ( $m_{prior}$ ), this information can be used to constrain the solution. When combining this with the LSQR, a weighting factor that expresses how much we trust our prior information is introduced. This factor is known as the damping factor (Maurer, 2017). For this case, a new objective function is formulated and when minimizing it, it leads to:

$$m = (G^T W_d^T W_d G + \alpha_s^2 I)^{-1} (G^T W_d^T W_d d + \alpha_s^2 I m_{prior}) \quad (5-10)$$

Where  $\alpha$  is a diagonal matrix with the damping coefficient in the main diagonal for the prior information of each parameter.

### Smoothing

On the other hand, another way of constraining the solution is by imposing on the structural feature. This regularization is also known as Occam inversions. There are many formulations of Occam's razor, but this can be summarised as simple models and theories are preferred over complex ones. This implies that the change for nearby points should be as smooth as possible for the structural case. This constraint is only helpful when the model parameters are a function of space ( $m = m(r)$ ).

We introduce a smoothing matrix  $W_x$  that can take many shapes to impose this constraint. Its importance in the minimizing scheme is controlled by a weighting factor  $\alpha_x$  in a similar fashion as  $\alpha_s$  did for damping. When introducing this factor in the objective function, the solution obtained can be expressed as:

$$m = (G^T W_d^T W_d G + \alpha_s^2 I + \alpha_x^2 W_x^T W_x)^{-1} (G^T W_d^T W_d d + \alpha_s^2 I m_{prior}) \quad (5-11)$$

## 5-2 Non-linear inverse problems

So far, we have only seen the case of a linear inverse problem that can be expressed as  $d = Gm$ . However, most geophysical problems are nonlinear. Looking at the Thomsen equations (3-10)

one can see that this is also our case. For this type of problem, the relationship between the observed data and the model parameters can be written as:

$$d = g(m) \quad (5-12)$$

This solution does not have a generalized inverse matrix  $G^{-g}$  as seen in the linear case and therefore we can not use the **LSQR** solution found in equation (5-6).  $g(m)$  is a forward function that calculates the theoretical response from model parameters and experimental geometry. The forward problem depends on an initial set of model parameters.

By a succession of approximation using **LSQR** technique the non-linear inverse problems can be solved (Yogeshwar, 2022). For that, we want to minimize the convex, continuous and differentiable objective function:

$$\phi(m) = (d - g(m))^T(d - g(m)) \quad (5-13)$$

Expanding  $g(m)$  in a Taylor series around a starting model  $m_0$  we obtain:

$$g(m) = g(m_o) + \frac{\partial g}{\partial m}(m - m_o) + \theta(m) \quad (5-14)$$

Which can be rewritten as:

$$g(m) \approx d_o + J\Delta m \quad (5-15)$$

Where  $d_o$  is the calculated data vector for the starting model parameters,  $\Delta m$  is the updated model parameters vector and  $J$  is the Jacobian or matrix of partial derivatives. This one can be written as:

$$J = \begin{pmatrix} \frac{\partial g_1(m)}{\partial m_1} & \dots & \frac{\partial g_1(m)}{\partial m_M} \\ \vdots & \ddots & \vdots \\ \frac{\partial g_N(m)}{\partial m_1} & \dots & \frac{\partial g_N(m)}{\partial m_M} \end{pmatrix} \quad (5-16)$$

The Jacobian shows how strong the model parameters  $m_j$  influence the response. It tells how sensitive  $g_i$  is to  $m_j$ . Therefore, partial derivatives are also called sensitivities. If  $J_{ij}$  is large, the influence is also large. The corresponding model parameter is poorly determined if a column has small values. Therefore, an experiment should be designed so that the sensitivities are as large as possible (Maurer, 2017).

The linearized equation can be written as:

$$\Delta d = J\Delta m \quad (5-17)$$

Comparing it with equation (5-1) we can see that they have the same form. Therefore, we can obtain the model parameters by using the same solution as for **LSQR**, by:

$$\Delta m = (J^T J)^{-1} J \Delta d \quad (5-18)$$

And in a similar way to equation (5-11), we can write:

$$m = (J^T W_d^T W_d J + \alpha_s^2 I + \alpha_x^2 W_x^T W_x)^{-1} (J^T W_d^T W_d d + \alpha_s^2 I m_{prior}) \quad (5-19)$$

An improvement of the model parameters can be obtained by iterative updating them. Replacing  $m_o$  by  $m_{new}$  the model parameter will approach  $m_{true}$ .

Comparing equations (5-18) and (5-5), it can be seen that linear and linearized problems are formally identical (Maurer, 2017). However, there are a few significant differences:

1. Non-linear inverse problems need iteration to find the solution while linear ones can be solved in a single step.
2. Matrix  $J$  is dependent on the initial choice of the model parameters, while  $G$  is independent.
3. The solution of the linear problem as it only requires matrix multiplication is computationally cheap, while the computation of the matrix  $J$  can be expensive.

### Data resolution matrix

Assuming we can solve the inverse problem, we can determine how well the updated estimated data fits the observed one. For that, we impose the following:

$$d_{pred} = N d_{obs} \quad (5-20)$$

Where we have introduced the data resolution matrix  $N$ . It can be seen that this one can be expressed as (Maurer, 2017):

$$N = J(J^T W_d^T W_d J + \alpha_s^2 I + \alpha_x^T W_x)^{-1} J^T W_d^T W_d \quad (5-21)$$

In the ideal case that the data is perfectly reproduced we have that  $R_d=I$ . Therefore, the closer the resolution matrix is to a diagonal matrix, the better the data is reproduced. This matrix is useful to analyze the importance of individual data points. The diagonal elements are referred to as data importance. A small value means a poor correlation between predicted and observed data, and a high one indicates an important point. Therefore, experiments should be designed for data points with a high importance value.



---

# Chapter 6

---

## Motivation

Seismic methods offer a good insight into the rock properties and the geological features between boreholes. In particular, Crosshole Seismics involves the placement of a source and one or more receivers in distinct boreholes. Once activated, the source emits a signal that travels through the subsurface and is recorded by the receivers. This shooting process is carried out at different depths. From the recorded signals, it is possible to determine the velocities of different wave types. With the given velocities it is also possible to derive elastic moduli for the rock between the boreholes as it varies with depth.

In this part of the thesis, we will focus on using crosshole seismic to characterize the anisotropy of the host rock. We will first look at a previous study using P-waves. Later we will determine the advantages of adding information from S-waves using inverse theory methods.

### 6-1 P-wave Crosshole Seismic

[Epiney \(2022\)](#) conducted a crosshole survey in the Bedretto laboratory to use P-waves time arrival to investigate the anisotropy in the Rotondo granite. She used SB2.1, SB2.2 and SB2.3 boreholes, located within the laboratory niche.

The short boreholes are filled with water, which makes necessary the use of source and receiver compatible with such conditions. In this case, a hydrophone chain of 24 channels with 1 m spacing was used, and as source, a Geotomographie GmbH SBS42 P-wave sparker was utilized. According to the specifications from the manufacturer ([Geotomographie, 2015](#)), this sparker is designed to produce a repeatable high-frequency compression P-wave signal. An impulse signal generated by the IPG5000 Impulse generator was required to activate the source.

With the collected data, the arrival times of the P-waves were manually picked and later utilized in an inversion scheme. By this, an approximation of the Thomsen parameters  $\epsilon$  and  $\delta$ , as well of the velocity of the P-waves in the direction of the symmetry axis  $\alpha_o$  and of the dip and azimuth of the symmetry axis was done. The resulting values are documented in table (6-1).

$\epsilon$	0.04
$\delta$	-0.3
$\theta_o$	109°
$\phi_o$	209.°
$\alpha_o$	5236.33 m/s

**Table 6-1:** Anisotropy parameters for the Rotondo grinite found by [Epiney \(2022\)](#).

### 6-1-1 Detection of S-wave Splitting

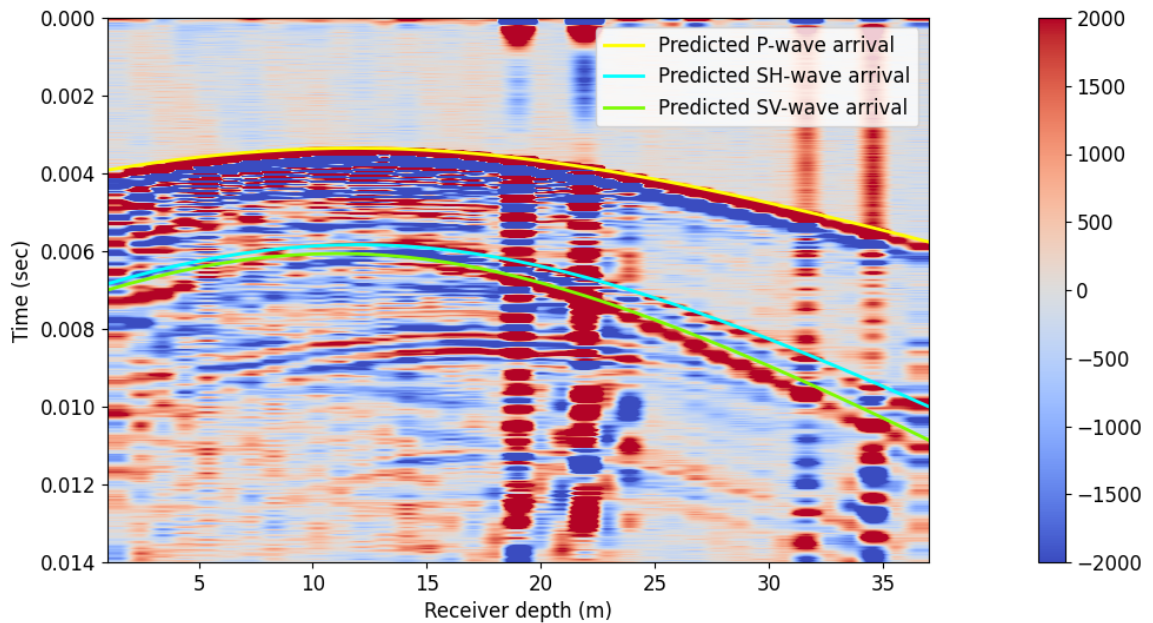
The data of this survey shows that the arrival of S-waves is easily observable. Interestingly, in specific borehole configurations, two distinct arrivals of S-waves were detected, indicating the presence of S-wave splitting. This phenomenon occurs in anisotropic media for specific ray directions.

Figure (6-1) shows a superposition of two data sets acquired by [Epiney \(2022\)](#) where the shot is in the same position in SB2.2 and the last receiver of the hydrophone chain was placed first at 37 m depth in SB2.3 and later moved to 24 m. Therefore, a shot receiver covering almost all the length of SB2.3 is obtained. The expected arrival of the different waves has been superimposed and to calculate them, the expressions in equation (3-17) were implemented as a Python function. Estimated values of the different parameters were provided and table (6-2) document them. These differ from those found by [Epiney \(2022\)](#) because since the study was completed, the parameters have been updated and there has been a change in the angle definition. There have also been some parameters that have been picked manually to get a better fit of the arrival times as no prior information on them was available. This is the case of  $\gamma$  and  $\beta$  as in the optimization carried out by [Epiney \(2022\)](#) those parameters were not found. It is known from literature that  $\gamma$  is primarily positive ([Tsvankin, 2012](#)), so with this information, we have tried to optimize its value until a good fit was obtained.

$\epsilon$	0.065
$\delta$	0.045
$\gamma$	0.09
$\theta_o$	17.15°
$\phi_o$	293.01°
c33	68.2e6
c55	21.7e6
$\rho$	2.6

**Table 6-2:** Values of the different parameters needed to do the calculation of the expected arrival time of the different wave types.

Additionally, information about the distance, dip, and azimuth of the rays for each shot and receiver configuration is required to compute the expected arrival times. The general Bedretto Lab model provides the specifications of the SB, which includes depth, easting, northing, and elevation along the borehole. We can import the other three parameters by knowing the depths at which the source and receiver are positioned in a borehole. Using trigonometric rules, it becomes possible to determine the dip, azimuth, and ray length using these parameters.



**Figure 6-1:** Shoot gather recorded from SB2.3 and shot from SB2.2 at a 16m depth along the borehole. The expected arrival time for the different wave types has been superimposed.

In figure (6-1), the calculated arrival times fit pretty well the observed signal. It is therefore reasonable to say that this phenomenon must be S-wave splitting. This thesis builds upon this fact, it is intended to study more in depth the behavior of S-waves in the host rock and try to understand the splitting. With these waves' information, we also want to improve the anisotropy model obtained by [Epiney \(2022\)](#) by adding the time arrivals of one or both S-wave types.

## 6-2 Sensitivity Analysis

A study on the sensitivities has been done to determine if the S-waves provide significant additional information on the anisotropy model. As seen in section (5-2), this can be obtained from calculating the Jacobian as in equation (5-16). The observed data obtained from crosshole seismic  $d$  are the travel times, and therefore the function  $g(m)$  is the analytical formulation of this time arrivals. The calculation of travel times can be performed using the formula  $t = \frac{d}{v}$ , where  $t$  represents the travel time,  $d$  is the known distance between the source and the receiver, and  $v$  denotes the apparent velocity of the seismic waves. The velocities are the ones obtained from using [Thomsen \(1986\)](#) equations.

To calculate the Jacobian matrix, we have computed the partial derivatives of the travel time for each of the model parameters. This has been done in a Python script and each row of the matrix has then been filled with specific shot and receiver positions setup. The setups used were the same as [Epiney \(2022\)](#) utilized for her project, as they cover most of the dip

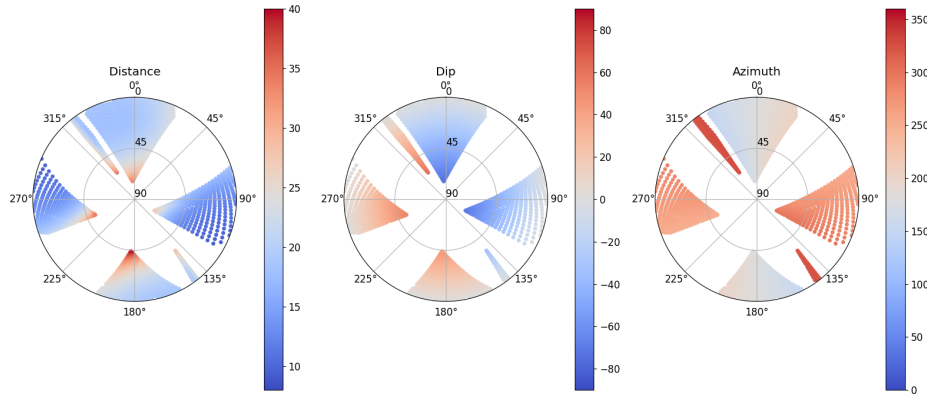


**Figure 6-2:** Distance, dip and azimuth of the ray of the survey conducted by Epiney (2022) and used for the sensitivity analysis.

and azimuths that the tripod can offer. The specific characteristics are shown in figure (6-2). The values used as the initial model parameters to compute the Jacobian matrix are the ones specified in table (6-2).

The matrix was filled sequentially, starting with the partial derivatives for P-wave velocity in the upper rows. To illustrate how it was calculated, let's consider one row of the matrix for P-wave. For the first column, we used the analytical derivative of the P-wave time arrival with respect to  $\alpha$ . By using the values of the model parameters along with the known dip, azimuth, and distance for a given source and receiver configuration, we compute the corresponding value of the Jacobian. This procedure was repeated for the other columns, with the different partial derivatives for the other model parameters. It is later followed by SV-wave derivatives obtained in the same manner, and concluding with SH-wave derivatives.

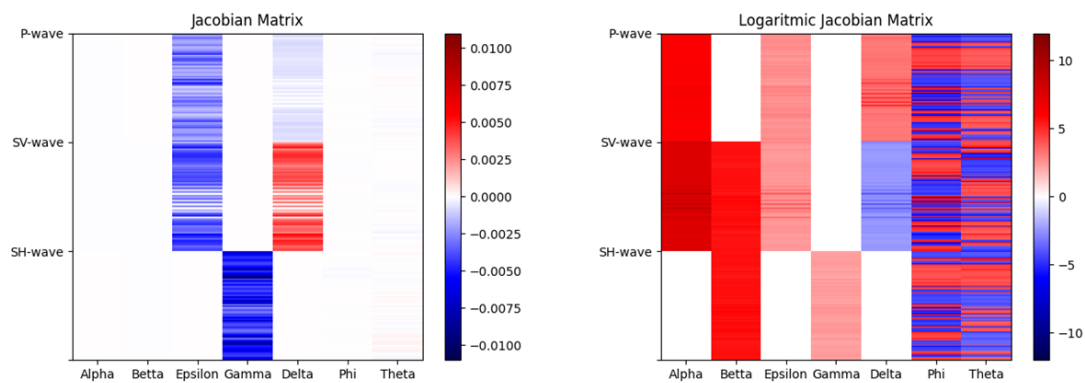


**Figure 6-3:** Left: Jacobian matrix. Right: Jacobian matrix using a logarithmic scale.

The left side of figure (6-3) shows the representation of the Jacobian matrix found for the specific used model parameters. The sensitivity is found to have a wide range, but many parameters are found to be relatively insensitive. We also encounter positive and negative values.

This indicates an increase or decrease respectively of the time of arrival when infinitesimally changing the value of the model parameter.

To enhance the visualization of the low sensitivity values of the Jacobian matrix, the logarithm of the absolute values of each element has been plotted, with the corresponding sign. The resulting plot is shown on the right side of figure (6-3). Since the logarithmic scale is used, sensitivity values less than one will be negative in this scale. In our case, all should have negative values. However, since we have also used the original sign of each sensitivity, negative sensitivity values are now represented by positive values. And counter-intuitively, those with high absolute values in this plot are the ones that produce a smaller change in the response when changing the parameter infinitesimally and therefore have a lower sensitivity.

The logarithmic scale representation of the Jacobian in the figure (6-3) shows that the sensitivity of some parameters is 0. This is because the seismic velocity of the three types of waves does not strictly depend on all seven model parameters. For example, in the case of P-waves, equation (3-10) shows that the velocity of this wave does not depend on  $\beta$  and  $\gamma$ . Consequently, the sensitivity of these parameters is 0. Modifying the values of these parameters will not impact the velocity of the P-wave, and therefore, it will not affect the arrival time.

Therefore, looking at the matrices, the following can be noticed:

1.  $\epsilon$  and  $\delta$  exhibit significant sensitivity for both SV and P-waves. For  $\delta$ , SV-waves have a higher sensitivity in absolute value and an opposite sign than P-waves. The difference in sign provides valuable information when the parameter increases or decreases, helping to characterize further and to constrain this parameter.
2.  $\gamma$  is also found to have high sensitivity for SH waves.
3. The parameters with the lowest sensitivities are  $\alpha$  and  $\beta$ , which are the velocities of the P and S-waves in the direction of the symmetry axis respectively. This implies that the model has a higher sensitivity to velocity changes outside the axis. This observation is reasonable as the exact direction of the symmetry axis is also unknown. If an arrival time measurement in this specific direction were made, it would provide better constraints on these parameters.
4. Most parameters either increase or decrease for a specific type of wave. However,  $\phi_o$  and  $\theta_o$  alternate between positive and negative sensitivity values. Interestingly, this alteration does not seem to have the same pattern for the different geometry setups for the different types of waves. Having information on the S-waves for these parameters would be desirable in the same way as for  $\delta$ .
5. Without the information provided by the S-waves  $\beta$  and  $\gamma$  are indeterminate.

As mentioned, each row in the Jacobian corresponds to a ray path and can be plotted in the stereonet. In figures (6-4), (6-5) and (6-6), the sensitivity of each model parameter is plotted on a stereonet for each wave type. Each point on the stereonet represents a specific ray path, and the point's color indicates how sensible a particular parameter is. These plots allow us to visualize how the sensitivity of each parameter varies for the different ray orientations

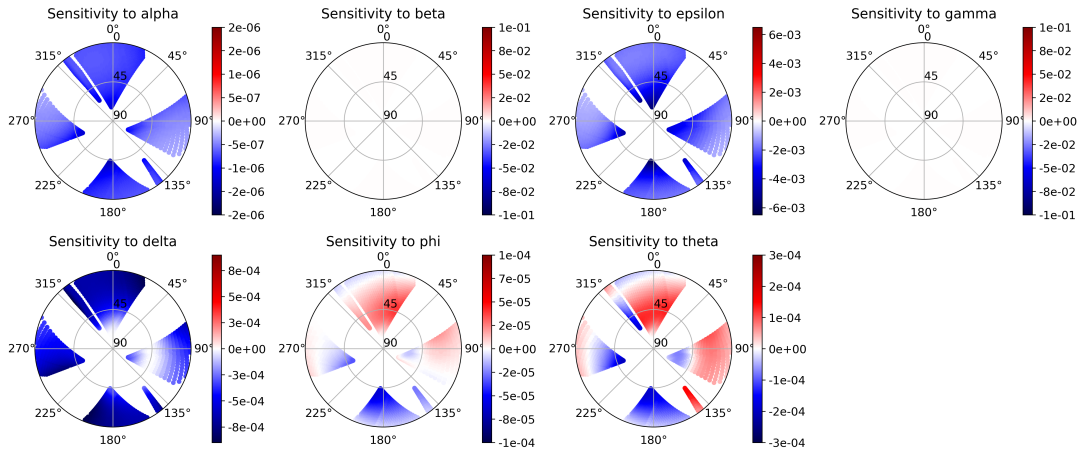


Figure 6-4: Sensitivities of the different model parameters for P-waves plotted in a stereonet.

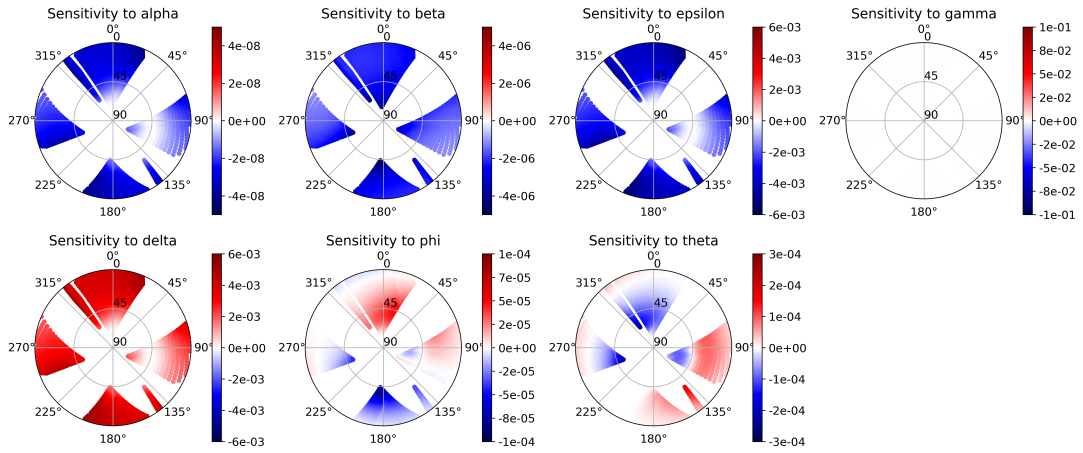


Figure 6-5: Sensitivities of the different model parameters for SV-waves plotted in a stereonet

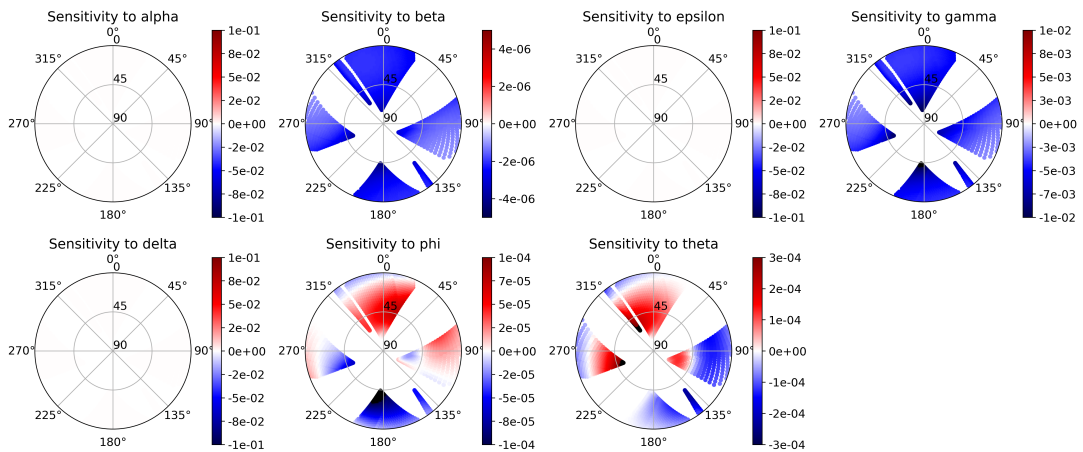


Figure 6-6: Sensitivities of the different model parameters for SH-waves plotted in a stereonet

and identify directions with higher sensitivity in the volume between the boreholes under consideration.

As mentioned earlier,  $\delta$  has a sensitivity with opposite signs for P and SV-waves. In the stereonet representation, it becomes noticeable that both types of waves exhibit a similar distribution of the absolute value of this sensitivity. Furthermore, we observe that  $\epsilon$  for SV-waves also has this distribution. This can be explained by looking at equation (3-10), where we notice that these parameters have the same dependence on  $\sin(\theta)^2\cos(\theta)^2$ , differing only in the values to which they are multiplied.

Another interesting observation is the similar sensitivity distribution that  $\phi$  has for the three types of waves. Also, with this representation, we can notice more easily that SH-waves have a higher sensitivity for this parameter. On the other hand, looking at  $\theta$ , we have a completely different trend. A similar pattern can be noticed when the sensitivity becomes zero for all the waves. When SV-waves we have that SH-waves are positive and the other way around. In contrast, for P-waves, the sensitivity distribution does not exhibit the same pattern as the S-waves.

### Data resolution matrix

As section (5-2) mentions, the data resolution matrix expresses which points give the most significant information. Certain parameters such as the Jacobian and smoothing/damping parameters need to be determined to calculate it. The Jacobian matrix has already been obtained in the previous section. The smoothing constraint is applied when model parameters are expected to vary spatially. As we consider them constant, we can set  $\alpha_x$  to 0. The damping parameter,  $\alpha_s$ , represents our confidence level in the initial model chosen. This parameter has no physical significance and has to be chosen by trial and error. However, no prior information is available for the model parameters other than the ones given to calculate the Jacobian matrix. That is why  $\alpha_s$  has also been set to 0. Lastly, the same error has been considered for all the data points in the weighting matrix. This error is the inaccuracy of manual picking, with a value of 0.05 ms.

Figure (6-7) shows the obtained data resolution matrix. Upon initial observation, it can be noticed that it is not close to a diagonal matrix as it is desirable to obtain. It is a symmetric matrix and a 3x3 division can be seen. The diagonal sections represent the influence of data points of the same wave type on each other. Sections outside the diagonal reflect the influence of data points from one wave type on those of another. For instance, sections 1,2 and 2,1 of the matrix correspond to how P-waves data points influence S-waves ones. To resolve a certain point, a linear combination of all the points of the corresponding row has to be done. Therefore, having a negative value means that this point has a negative influence on such a point. From figure (5-21) we observe that data points from the same wave type play a more significant role in determining a certain point's resolution than negatively influence those from a different wave type.

In figure (6-8), the importance of each point is plotted on a stereonet being these the diagonal values of the data resolution matrix. They indicate how much weight a data point has on its own prediction and they represent the reproducibility of such point. Therefore, higher values of importance are more valuable. It can be observed that the importance values are generally low, far from the ideal situation. This suggests that the data resolution

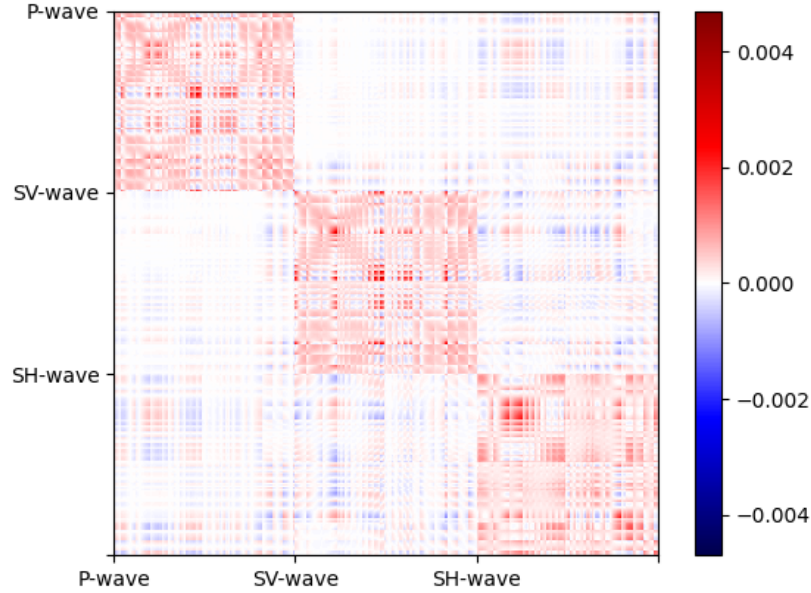


**Figure 6-7:** Data resolution matrix.

is not optimal and that points can not be predicted on their own but as a linear combination of the other ones. It can also be noted that the points with the highest importance are concentrated in a specific range of dips between  $50^\circ$  and  $65^\circ$  and  $-65^\circ$  and  $-50^\circ$ . It is worth recalling that a ray with the same azimuth and opposite dip is plotted at the same point in the stereonet. Therefore, both ranges of dips are plotted one on top of each other. Finally, it can be seen that SV waves have slightly higher importance values than P-waves and that SH-waves exhibit the lowest values.

In this section, we aim to assess if S-waves provided significant complementary information. We have found that without such information,  $\beta$  and  $\gamma$  parameters are not defined, making it challenging to interpret the seismic signals for these waves correctly. Additionally, we observe that  $\delta$ , and  $\phi$  parameters exhibit positive and negative sensitivities, providing valuable information to constrain them better. The importance of each data point was also studied. However, the difference between the values obtained for SV-waves and those obtained for P-waves is not significant enough to conclude that they are better at predicting themselves.

Overall, with this theoretical approach, we have seen that incorporating information from SV and SH-waves is beneficial to characterize the anisotropy and to make the approximations obtained more robust. Therefore, in the following stage of our study, we will focus on practically incorporating such information.

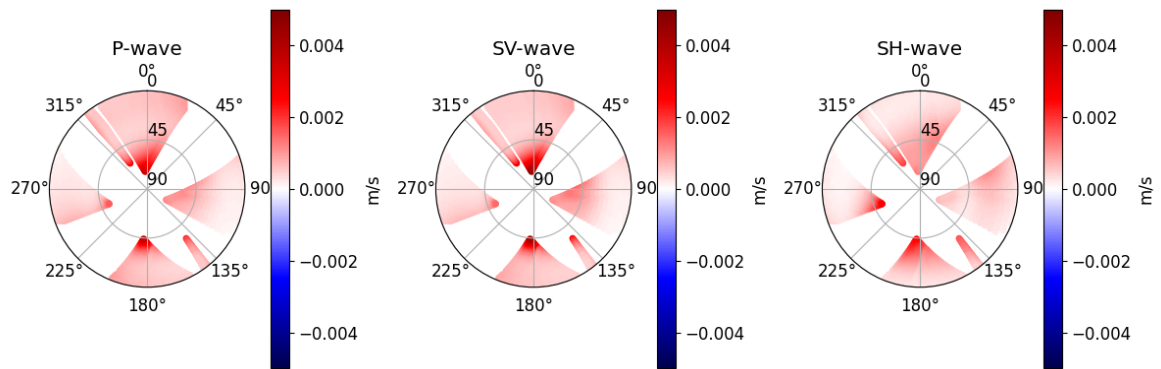


**Figure 6-8:** Importance of the data resolution matrix plotted in the stereonet.



# S-wave Characterization

In chapter (6) two types of S-waves have been detected and we have found that the information they provide is meaningful for a more accurate anisotropy model. In this chapter, we will discuss the different approaches that we have tried in chronological order to understand the behavior of such waves to manually pick the time arrivals of the two types of S-waves.

## 7-1 S-wave Sparker

The investigation of the S-waves led us to the BIS-SH borehole source, manufactured by Geotomographie, as a first step. The instrument specifications indicate that it generates a repeatable polarized signal resulting in one type of shear wave and the compressional one (P-waves) (Geotomographie, 2015). The BIS-SH source is designed to operate in both dry and water-filled boreholes. For its use, it must be coupled to the borehole wall. A pneumatic clamping system is utilized to secure the sparker in place during operation. When inflated, this system holds the sparker, preventing any movement. This instrument also requires the IPG5000 Impulse generator to be used.

On March 27th, a survey was conducted using the S-wave sparker and the 1 m spacing 24 channels hydrophone chain. The receivers were positioned at SB2.3 while the source was at SB2.2. The chain was placed at two different depths, the first one had the last receiver at 38 m while the other had it at 24 m. For each of the two last receivers' depths, three different source depths were used: 10, 24, and 38 m. To better understand the type of waves it generates, the instrument was rotated around its own at each depth position. For each depth and rotation position, at least four shots were made and each was saved in a SEG-2 data file.

### 7-1-1 Data Processing

This study utilized Python for all data reading, plotting, and processing. The obtained file contains the recorded amplitudes of the 24 channels of the hydrophone chain as a function of

the sample point. Later, these amplitudes can be converted to time by knowing the sample rate. During the recording process, a short time before the triggering of the source is always captured. Therefore, the first processing step involves trimming the trace to remove this time. Afterward, the data is prepared for plotting, providing an initial evaluation of the raw data.

There are two main approaches for plotting the data. The first option is to create a plot showing the amplitude of each trace of the shot gather as a function of time. The other option is to visualize the shot gather with a color function. For this one, the color depends on the sign of each data point while the intensity of the color depends on its relative amplitude.

A first check of the raw data showed that certain traces exhibited a low-frequency signal throughout the entire recording duration, covering the desired signals (figure (A-1) left). A highpass filter was applied to remove this unwanted component, where all frequencies below 60Hz were discarded. Following the filtering, the arrivals of the different waves became more distinct (figure (A-1) right). Additionally, the data was stacked for the shots recorded in each source and receiver position for each rotation step, to improve the signal-to-noise ratio.

## 7-1-2 Results

Figure (7-1) presents the results of the S-wave sparker for a specific source position. The expected arrival time of the different waves has been superimposed in the same way as in figure (6-1). As previously mentioned, the sparker was rotated at multiple steps. In figure (A-2), the cable orientation at the top of the borehole can be observed for each rotation step. At first glance, it becomes apparent that the S-wave sparker signals are not as clear as the P-wave sparker. Noticeably, the signals exhibit a fading effect in the rightmost traces, which correspond to the farthest distances from the source.

We can observe distinct behavior of the waves based on the source position. Firstly, let's concentrate on the P-waves. At rotation steps 11, 12, 13, and 14, we observe a positive amplitude for the wave arrival. However, this amplitude fades slightly for rotation 15 and becomes negative for position 16 (indicated by the blue first arrival). Lastly, a positive amplitude is observed again at rotation step 17.

Next, we will examine the behavior of the S-waves. At rotation step 11 and 12 we have a strong signal for what we would expect to be the arrival of SV-waves. On the other hand, for rotations 13 and 14 we see a stronger signal for the arrival of SH waves, while still detecting SV-waves. As we rotate the source further, positions 15 and 16 exhibit a strong signal for SH-waves, but no significant one for SV-waves is observed. Finally, for the last rotation, we still detect a strong signal for SH but the arrival has a negative amplitude.

Similar results were observed for other depth positions of the source along the borehole, but not all of them show a change in the polarity or wave type. This discrepancy is likely attributed to the uncertainty regarding the successful rotation of the sparker. When attempting to change the source orientation, the cable of the sparker was rotated at the surface, but it remains unclear if the rotation effectively propagated along the cable. As a result, a more comprehensive study of the source's operation could not be made with certainty.

The most significant finding of this study is the observation of different types of S-waves in different directions. These waves show distinct variations in amplitude and polarity, indicating different particle motion characteristics. This suggests that isolating both types of waves could

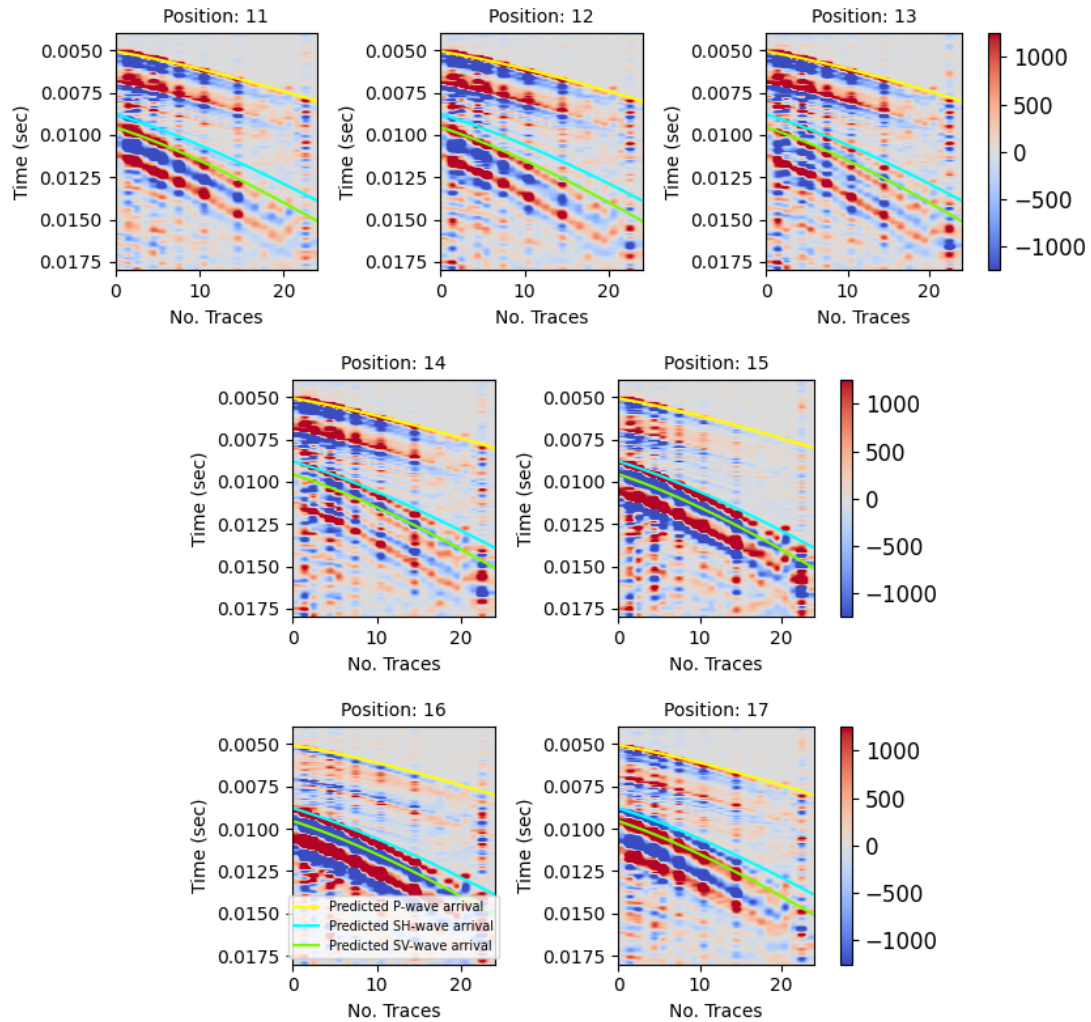


**Figure 7-1:** Shot gather using the S-wave sparker for the 7 different rotations of the instrument around its own. The source was placed at a depth of SB2.3 at 38 m, and the receiver was at 24 m in SB2.2.

be possible if the direction of propagation for each wave is known. One approach to achieving this is by recording the wave in multiple components. It is expected that each component will have a preference for either SH or SV-waves. By rotating the collected data, it should be possible to separate each type of wave into one component.

## 7-2 3-Component Geophone

The 3-component geophone BKG3, manufactured by Geotomographie, records three mutually orthogonal components (Geotomographie, 2011). The geophone is secured to the borehole wall with a clamping system that uses two pistons to hold it in place. According to the manufacturer, the sensor's assembly generates a positive rising signal in the direction aligned with the sensor's orientation. This information is useful to interpret the recorded signals and understand the polarity of the waves.

### 7-2-1 Hammering Test

On April 27th, a first test was conducted using the BKG3 geophone. It was positioned in the SB2.3 borehole, which has the same azimuth as the tunnel rail. The vertical component of the receiver was in the direction of the borehole and the horizontal components were in a plane perpendicular to it. The energy source was a hammer, and the procedure consisted of hammering the tunnel floor at 1 m intervals. We also hammered the right and left sides of the tunnel rail, intending to generate S-waves. We tried to repeat the procedure at another depth in the borehole. However, the geophone failed to attach properly to the borehole wall. Upon inspection, it was found that the instrument was leaking air, preventing us from making further measurements.

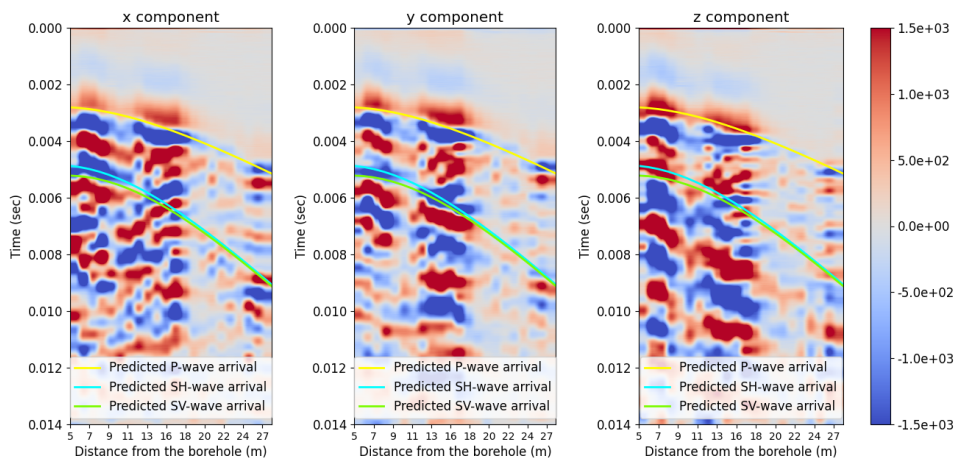


**Figure 7-2:** Receiver gather when the 3-component geophone was placed in SB2.3 using a hammer as a source.

The 3-component geophone generates three traces per shot, one for each component. These traces can be plotted simultaneously or displayed as receiver gathers for each component. The

latter approach was selected to present the results of this study. Figure (7-2) illustrates the outcomes of hammering the tunnel's ground. The recorded signal appears not to be very sharp and clear. Despite attempts to enhance the quality by stacking the different shots at a source and receiver position and filtering, no improvement was achieved. It is thought that the poor resolution of the data could be due to a bad coupling of the geophone to the borehole wall. It could be that the instrument was already leaking in the first receiver position. Another possibility could be the source choice. A hammer is not a repeatable source. Therefore stacking does not necessarily improve the quality of the data. Also, the propagation of the waves through the first meters of the tunnel is more complex than for the volume between boreholes. This is because it is a half-space where the stress field is perturbed and because the first meters are cemented.

Figures (A-4) and (A-5) show the results for the case where the side of the rail was hammered. The images quality is similar and do not give significant information either.

### 7-2-2 Crosshole Seismics

A month later, on the 27th of April, a second attempt to measure with the 3-component geophone was made. This time, we conducted crosshole seismic with the source at SB2.2 and the receiver at SB2.3. These two boreholes are contained within the same plane, resulting in no azimuth variation for the ray paths, only in dip. The P-wave sparker was selected as the source.

During this survey, the geophone was deployed at two different depths: 10 and 24.8 m. The source depth was varied from 5 to 29 m (figure (A-6)). The vertical component of the geophone was aligned with the borehole, while the other two were in a plane perpendicular to it. To determine the orientation of the two horizontal components, a sensor providing information on the dip and azimuth was attached to the geophone. A summary of the information for this survey can be seen in the table (7-1).

	Source BH	Receivers BH	Source depth (m)	Receivers depth (m)	Receivers azimuth (°)	Receivers dip (°)
Position 1	21	23	5 - 29	24.8	326	-70
Position 2	21	23	29 - 5	10	60	-73

**Table 7-1:** Specifications of the crosshole seismic carried using the 3 component geophone.

### Raw data

The data obtained in the second test proved to be more satisfactory than the initial one (figure (7-3)). Only time trimming and stacking the data was done and again a receiver gather was used to plot the data. The vertical component of the geophone (z-component), shows slightly less sharpness than the x and y-components. However, it still reveals a significant observation: the first arrival of the signal does not align with the expected P-wave arrival, indicating again that the wave's energy does not propagate in all directions.

In the x and y-components of the geophone at the receiver depth of 10 m, distinct wave behaviors are evident. For the x-component, a positive amplitude for the P-wave is observed,

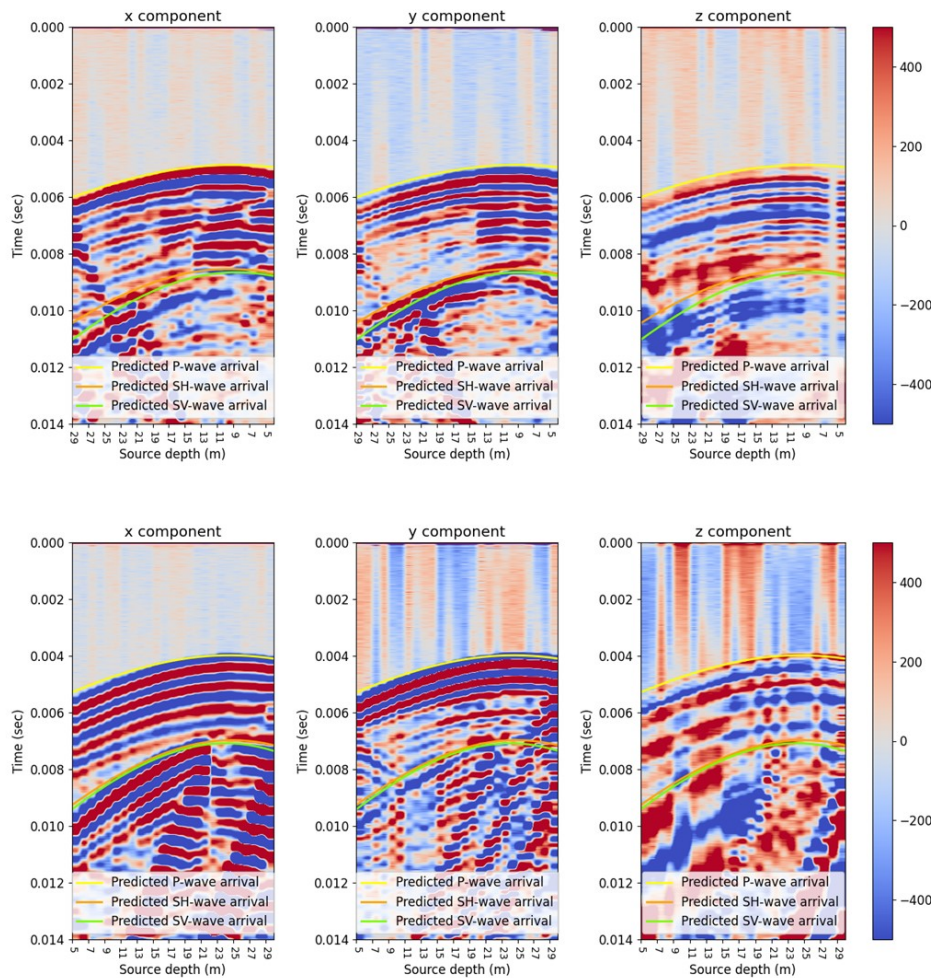


**Figure 7-3:** Receiver gather of raw crosshole seismic data using a 3-component geophone. The upper image corresponds to a receiver depth of 10 m while the second one corresponds to 24.8 m.

while a negative one is obtained for the y-component. Furthermore, the y-component also shows a signal corresponding to the expected arrival time of SH waves. On the other hand, the x-component shows a more pronounced signal for the arrival of SV waves.

When considering the receiver gather of 24.8 m depth, both the x and y-component exhibit a negative amplitude for P-waves. However, only in the y-component is the S-wave visible but it can not be differentiated which of the two types it is as no significant splitting is expected to be detectable.

With this newly collected data, we can demonstrate again that detecting the different wave types depends on their propagation direction. The propagation of the energy of a wave is no longer in the direction of the propagation vector. Instead, each wave has a different energy propagation direction, therefore we can distinguish them for different components. In order to achieve the desired outcome of having each wave's maximum in one component, we

need to determine the direction of energy propagation and rotate the data obtained from the 3-component geophone accordingly.

### Data rotation

To isolate the different waves, two rotations have been carried out. The first rotation involves rotating around the y-component of the geophone. To achieve this rotation, the following matrices have been used, which produce an hourly rotation around the axis:

$$R_y = \begin{pmatrix} \cos(\alpha) & 0 & -\sin(\alpha) \\ 0 & 1 & 0 \\ \sin(\alpha) & 0 & \cos(\alpha) \end{pmatrix} \quad (7-1)$$

$$R_z = \begin{pmatrix} \cos(\beta) & \sin(\beta) & 0 \\ -\sin(\beta) & \cos(\beta) & 0 \\ 0 & 0 & 1 \end{pmatrix} \quad (7-2)$$

Where  $\alpha$  and  $\beta$  are the rotation angles around the y-component and z-component respectively. To obtain the rotated data ( $D_r$ ) from the original data ( $D$ ) the following expression is used:

$$D_r = R_z R_y D \quad (7-3)$$

Different combinations have been tried and the angles that best isolate each type of S-wave in one component have been found visually. The  $\alpha$  angle that gives better results has been found that places the y and x-components within the propagation plane of each ray. To do this, each trace has been rotated individually as each had a different dip. The rotation around the z-component has been found to be most successful when orienting one of the horizontal components parallel to the ray propagation direction. Since the rays between SB2.3 and SB2.1 are contained in the same plane, this rotation does not need to be done trace by trace. Instead, the same rotation is done for the entire receiver gather.

Looking at the receiver's gather after being rotated, it becomes apparent that for the receivers at 10 m, there is a good separation of the two types of S-waves. We can detect SH for the x-component while SV-wave can be seen in the y-component. However, for the recordings at 24 m, where no significant splitting is expected, we have not been able to distinguish between the two types of wave. The results are promising and it is believed that if more data was collected it would be possible to isolate these waves for zones with sufficient splitting.

## 7-3 Full 3-component Geophone Survey

After the successful result in isolating the S-waves, as described in section (7-2-2), a more extensive survey was conducted on the 4th, 5th, and 6th of July. For this survey, an 8 receiver chain with 2 m spacing consisting of BKG3 geophones was used. An inflatable pneumatic system was used instead of the cylinder clamping system this time. As source, a P-wave sparker was used once again. For the survey, a wide range of dips and azimuths of the rays was covered by moving the receivers along the boreholes. An intensive coverage was made

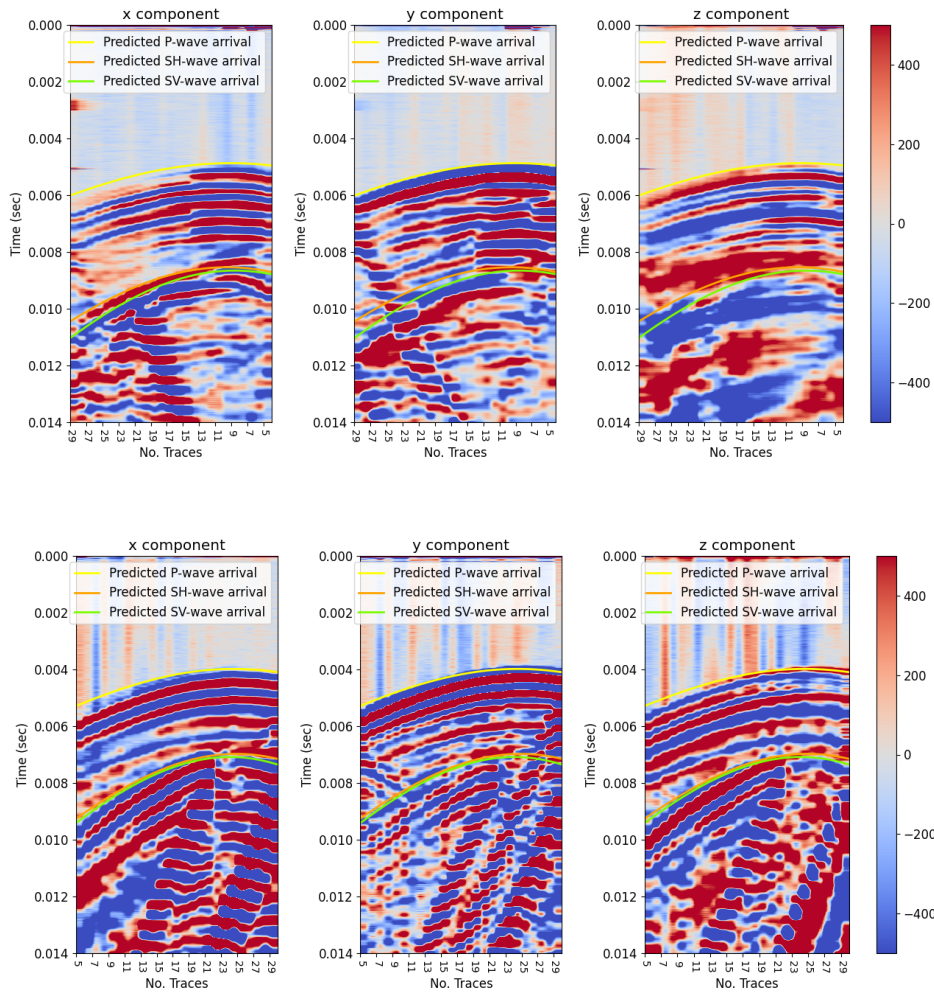


**Figure 7-4:** Receiver gather of the stacked and rotated seismic data. The upper image corresponds to a receiver depth of 10 m while the second corresponds to 24.8 m.

with 1 m spacing in the plane from SB2.3 to SB2.2, as it is in this region where we expect more splitting. In the other two planes, a 2 m spacing was done.

During the first day, some challenges were encountered with the pneumatic clamping system and one of the receivers was lost. On the second day, a problem with the triggering was encountered. It was starting recording at inconsistent times for each shot. Fortunately, this problem was not haven on the third day. During the whole survey, there was a channel that was not recording signals correctly and occasionally a second one that was recording lower frequencies than expected or sometimes not recording at all. On the second day, further issues with the pneumatic systems were encountered, which led to the loss of two other geophones.

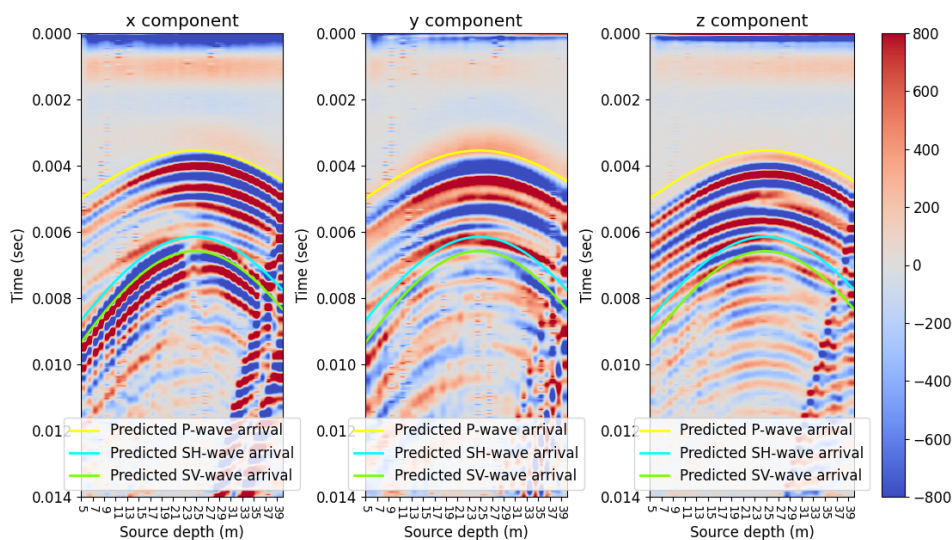
When placing the instrument into the borehole, the orientation of the horizontal components was unknown and it is also uncertain if each receiver had its own orientation. Once again, we used three receiver gathers, one per component, to plot the data. However, due to the issues

with some of the tracers, certain components in the receivers contain no information (figure (A-7)). We attempted to use shot gathers to plot the data. Nevertheless, as each receiver had a different orientation when placed in the borehole, the polarity of the different waves was not always the same, making the signals unclear and more difficult to interpret.

### 7-3-1 Data Processing

The first processing step was aligning the data and determining the correct time 0 for all the shots recorded during the first day of recording. An optimized procedure was found using the crosstalk, a spike caused by the high voltage created by the generator IPG5000 at the real time 0. Stacking the traces from the same shot enhances the spike and the data before a certain threshold, corresponding to the spike, is trimmed.

A high pass filter was utilized to eliminate the low-frequency noise present in certain channels, which removed all frequencies below 100Hz. Lastly, the data was stacked for the different shots taken at each source and receiver position to increase the signal-to-noise ratio.



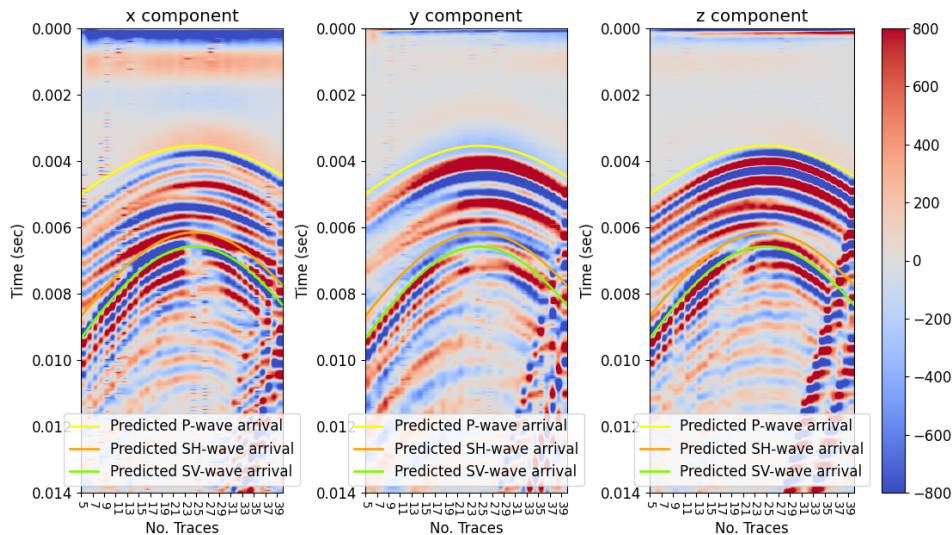
**Figure 7-5:** Receiver gather with the 3-component geophone placed at 22 m depth in borehole SB2.2 and shots were made at SB2.3.

Figure (7-5) shows an example of a receiver gathering after processing. It can be seen that in the recording x-component a strong signal for the S-waves. It can also be seen that the signal has a polarity change around the shoot at 23 m depth.

### 7-3-2 Rotation

In this survey, a Python script was created using the rotation matrices presented in the previous section. The script automatically searches for the optimal angles  $\alpha$  and  $\beta$  that maximize the amplitude of SH-waves in the x-component and SV-waves in the y-component for a specific receiver gather.

In this case, different angles were not used for each trace of the gather, as in section (7-2-2), but rather, the same angles were tried for the three components for all the receivers in the same chain position. It was successful in some cases, but specific angles for each receiver had to be used for others. By doing this, a better result was obtained and the different waves were isolated.



**Figure 7-6:** Receiver gather after being rotated where the 3-component geophone was placed at 22 m depth in borehole SB2.2 and shots were made at SB2.3.

Figure (7-6) shows the same receiver gather as in figure (7-5) after being rotated. Now it can be appreciated a signal in the y-component for the SV-waves in addition to the one of SH in the x-component. The script created was successful in most of the cases to isolate both types of S-waves except in areas where little splitting was expected.

After rotating the receivers, each component was saved in a .txt file containing information about the specific shot-receiver configuration. The file includes details such as the depth at which the receiver was placed in the borehole, the specific shot depth and for each shot, the dip, azimuth, and distance of the ray. The file can now be imported into the picking tool.

### 7-3-3 Picking

To obtain the travel times of the S-waves, a Python script was made to do the picking. The script, reads and plots the rotated data saved in .txt files, displaying it in an interactive interface. By clicking on the plot, the sample point for the arrival of each shot is saved. This can later be transformed into time knowing the sample rate. The picks are checked and later exported to a .txt file with its corresponding geometry information.

For the SH-waves, more picks were obtained as in zones where we expect to have small splitting, isolating both wave types was not possible and SV wave could not be differentiated.

Figure (7-7) shows an example of a receiver gather where the travel times have been picked. A polarity change can be noticed around shot number 10. However, an interesting observation

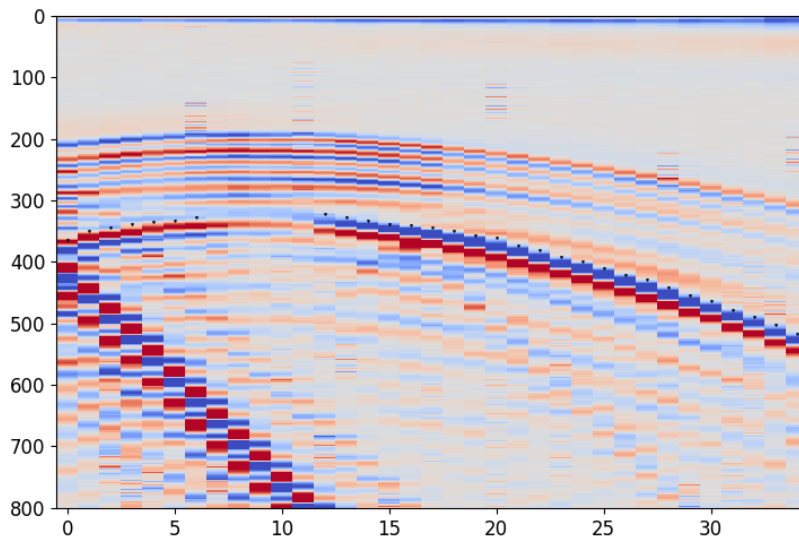


**Figure 7-7:** Receiver gather with the travel times picked for when the receiver was placed at 29 m depth in borehole SB2.2 and shots were made at SB2.3.

arises from the continuity of the red signal starting on the left side and appearing to extend to the right side. This raises uncertainty regarding our assumption of a polarity change. It is possible that the blue signal on the right side is not strong enough on the left side and we might have misinterpreted it as a polarity change. Further investigation and analysis are needed to confidently interpret this effect and understand the true nature of the signals in this region.



---

# Chapter 8

---

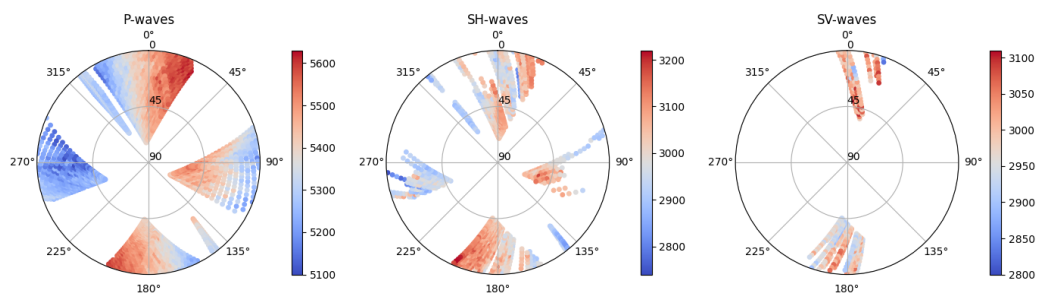
## Results

In the upcoming chapter, we will present the obtained results. We will discuss the apparent velocities found and the inversion of the model parameters.

### 8-1 Apparent Velocities

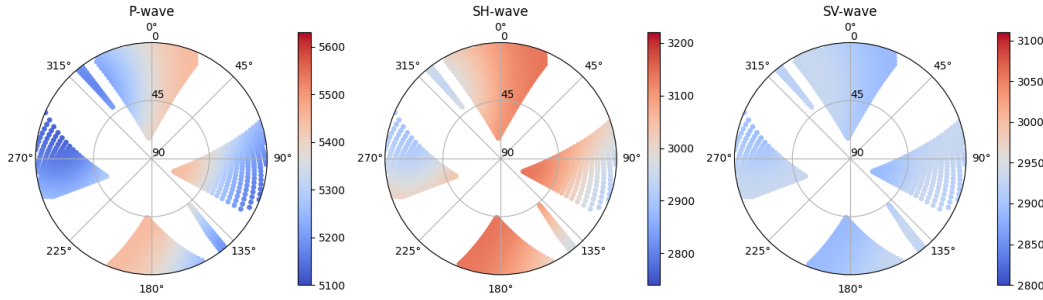
After manually picking the travel times, the velocities can be computed. Given that we know the distance each ray travels based on the geometry of the boreholes, the velocity can be calculated using the formula  $v = d/t$ . By associating the velocity of each wave to the dip and azimuth of the ray, we can display them using the stereonet representation.

Figure (8-1) shows the distributions found for SH and SV-waves as well as the one found by [Epiney \(2022\)](#) for P-waves. It reveals that velocity for the SH-waves varies from 2747 m/s to 3216m/s, and from 2830m/s to 3105m/s for SV-waves. We observe a higher velocity for the SH in the plane between SB2.3 and SB2.2. For SV-waves, only information for this plane is obtained. The lowest velocities are found in the plane between the SB2.1 and SB2.2 boreholes for SH-waves. We expect to find similar velocities for SV-waves to those found for SH in this plane and the one between the boreholes SB2.1 and SB2.3 as no significant splitting is detected.



**Figure 8-1:** Velocities measured from the picked times arrivals.

Noticeably, our coverage is not as extensive as that achieved by [Epiney \(2022\)](#). This difference in coverage is due to our utilization of 1 m spacing only for planes SB2.3 and SB2.2, whereas we used 2 m spacing for the other two planes. In contrast, [Epiney \(2022\)](#) used a 1 m spacing throughout. Additionally, it is more difficult to identify S-waves than P-waves as the compressional ones are the first signal recorded. On the other hand, S-waves can be challenging to differentiate from the P-waves tail or reflections, resulting in fewer data points.



**Figure 8-2:** Predicted velocities using the model parameters in table 6-2

Figure (8-2) presents the expected velocities for the model parameters in table (6-2). Comparing the predicted velocities with the obtained ones reveals a good fit for P-waves, indicating that the model parameters successfully predict this type of waves. Although, for SH-waves, the agreement is not as strong as for P-waves it still shows a good fit. However, due to not continuous velocity gradient seen in the apparent velocities for SH-waves is hard to interpret how good the fit is. Additionally, the apparent velocities for SV-waves appear higher than the predicted values. Also, a slight trend can be observed for this type of waves, although the limited coverage makes it challenging to conclude that.

Overall, the apparent velocities fit pretty well the predicted ones for SV and SH-wave velocities. However, the discrepancies in values and trends found suggest that the model parameters can be further improved to describe these waves adequately. By utilizing these observed velocities, a better anisotropy model can be found, leading to a better understanding of the properties of the Rotondo granite.

## 8-2 Inversion

The inversion aims to determine the model parameters that characterize a TTI medium. In chapter (5), we have seen the solution obtained through an iteration process using the Jacobian matrix. However, in this study, we opted for a different approach where the Fmin Optimization is implemented using a Python code. This method optimizes an objective function by comparing the given initial velocity model with the apparent velocities we have measured and adjusts the parameters to minimize the misfit between the two. This uses a downhill simplex algorithm, which might not be as accurate in finding the global minimum as the case of the iterative process seen in chapter (5). To mitigate this, the initial model should be as close to the observed velocities as possible.

The initial model given to the optimization script is documented in table (6-2). The function to be minimized is the sum of the misfits for the three waves from the apparent velocities

and the model ones. The function is provided with the apparent velocities found for SH and SV-waves in the previous chapter and those found by [Epiney \(2022\)](#) for P-waves. The apparent velocities for the three types of waves can be seen in figure (8-1).

$\epsilon$	-0.038
$\delta$	-0.061
$\gamma$	0.030
$\theta_o$	35.9°
$\phi_o$	315.5°
c33	79.8e6
c55	22.6e6

**Table 8-1:** Values found for the model parameters after the optimization procedure.

The optimization procedure generated an TTI model based on the apparent velocities. The model parameters found can be seen in table (8-1). From other studies, it is known that  $\epsilon$  and  $\gamma$  are often found to be positive. This implies that velocities in planes perpendicular to the symmetry axis are faster than those parallel to it for P and SH-waves. It was also found by [Epiney \(2022\)](#) that  $\epsilon$  is positive. However, the model's obtained value for this parameter is negative, making it less reliable due to mismatch. The corresponding velocities obtained when using the obtained values can be seen in figure (8-3). It can be noticed that the new model does not describe the velocities for different orientations for P-waves as well as the initial model parameters did. However, for the SH-waves it can be seen that the new model reasonably well recreates their distribution. It can also be observed that there is a distribution of velocities depending on the ray direction for SV, as can be seen in the apparent velocities.

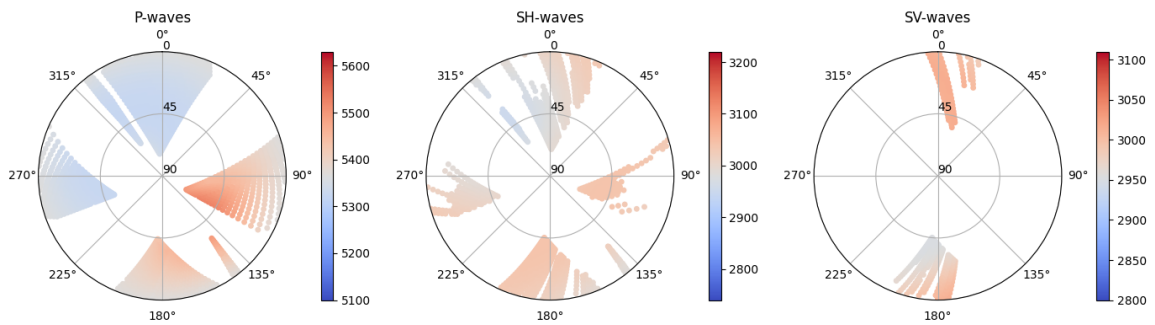


**Figure 8-3:** Velocity distribution using the model parameters obtained after optimization.

In figure (8-4), we see a great discrepancy between the values obtained by the new model and the apparent velocities in the P-waves. This is expected since the new model does not satisfactorily recreate the observed velocities of the waves. On the other hand, SH and SV-waves have a smaller error. Overall, although figure (8-5) shows that the residuals between the apparent velocities and the obtained model are smaller than the initial one, this is not a satisfactory model. It cannot provide a pattern of velocities depending on the ray direction compatible with the apparent velocities.

The approach used to find the model parameters is not satisfactory and specific changes are

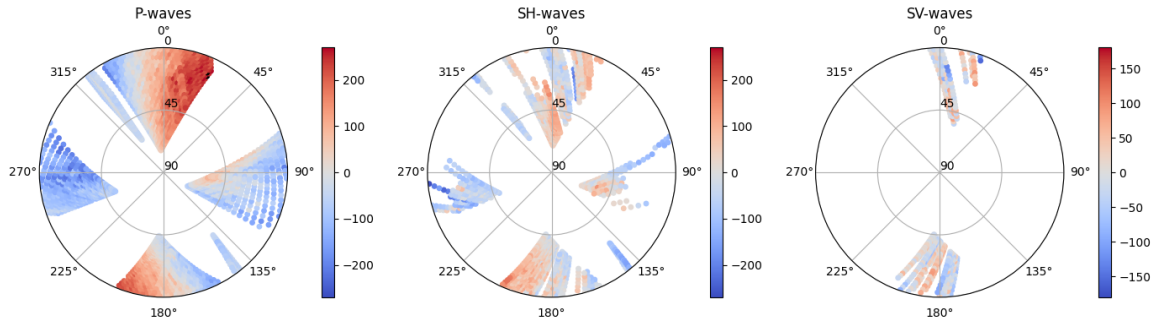


**Figure 8-4:** Difference between the apparent velocities and the obtained with the optimized model parameters.

necessary. In a new attempt to find the model parameters, a weight factor can be given to how confident we are of our observed data. For example, the information provided by SV-waves is not as reliable as the provided by P-waves. This is because, for the former, the picking is not accurate. In most cases, it is necessary to rotate the data to isolate them, and picking is more difficult for this wave as it interferes with reflections in the medium or with the tail of the SH and P waves. These are some of the factors that make this information less reliable and that should be considered. The inverse approach seen in chapter (5) offers a solution for that and would be a good option to have a more accurate model.

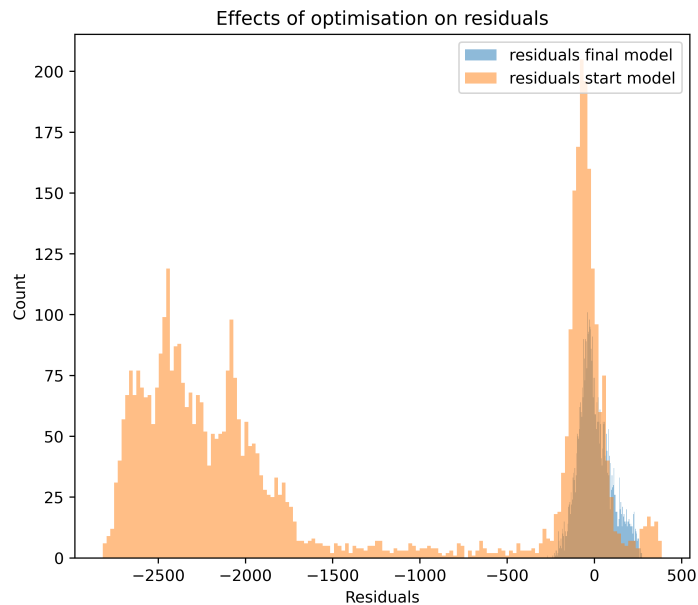


**Figure 8-5:** Histogram of the residual for the initial model parameters and for the obtained ones from the optimization procedure.

---

## Chapter 9

---

# Conclusion

In this project, we have presented a qualitative description of the anisotropy of S-waves in the Rotondo granite. First, we had a more theoretical approach where we determined that the S-waves provide significant extra information. It was found that S-waves are not correctly predicted without this information, making it difficult to interpret the seismic recordings from monitoring. Afterward, with different crosshole surveys, the behavior of the propagation of the different waves has been tried to study. We have successfully obtained a velocity distribution of both SH and SV-waves for different ray orientations. However, no model parameters that satisfactorily recreate the apparent velocities for different rays orientations were found.

It has been seen that **TTI** model can recreate the observed data successfully to a good extent. However, this is a simplification of reality and is therefore not perfectly accurate. Additionally, the findings might be influenced by assumptions or limitations in the data. These factors could introduce some misinterpretation and uncertainty in the results. Therefore, being aware of these factors is crucial. We will list the most important ones and possible outlooks that could improve the current understanding of anisotropy.

One significant factor contributing to inaccuracy is the uncertainty in the borehole trajectories. As depth increases the error becomes more pronounced and propagates to inaccuracies in determining the dip, azimuth, and distance of the rays. Subsequently, it impacts the calculation of the apparent velocities and their position in the stereonet representation.

Another assumption that was made is that there are no heterogeneities in the volume between the boreholes under consideration. We know that they avoid major faults, but there could be some fractures. We are not completely aware of how that could affect the propagation of the waves. It could be that the ray path between the source and the receiver changes as discontinuities could influence it. The existence of faults could be studied by doing a crosshole tomography, but due to the dipping of the boreholes, it is a challenging setup.

A limitation of this project is the lack of information about the orientation of the 3-component geophones. A more accurate interpretation of the anisotropy could have been done if this had been known. With this information, simulations could have been performed to replicate the results obtained and further validate the findings. Additionally, seeing if the simulations

show the polarity change we have detected in the S-waves would be beneficial for the picking process. It would provide clarity on the appearance of the signals we are trying to pick, leading to improved apparent velocities.

The effects of anisotropy in the Rotondo granite have been successfully seen and quantified. Nevertheless, the cause of it or how strong it is, is still unknown. [David et al. \(2020\)](#) found from laboratory measurements that the host rock shows a moderate low level of anisotropy. They also stated that it could be due to a high micro-crack density. These cracks are not randomly oriented and occur after the failure of brittle rocks during compression ([Sayers and Kachanov, 1995](#)). While laboratory and in-situ conditions may not perfectly align, it is reasonable to assume that the anisotropy observed in the Rotondo granite results from the stress field. The maximum velocity for fracture-induced anisotropy is parallel to them ([Holmes et al., 1993](#)). Therefore, a more comprehensive study could be done by combining the obtained information with the knowledge of the fractures' orientation and stress conditions.

Another aspect with potential use for further investigation is the orientation of the geophones during the data collection. If it was known, it would be possible to determine the orientation of the highest energy for each type of wave is found. With this information, it could be possible to understand how the energy radiates for an anisotropic medium compared to ray propagation. In addition, if we combine this data with stress conditions and micro-cracks' orientation, we can better understand anisotropy in the studied rock mass.

Lastly, in future studies, a better inversion scheme could be utilized to derive the model parameters using the apparent velocities that were obtained. This can be achieved using an iterative method like the one presented in chapter (5). This one offers the possibility to give major weight to data points that we think are more accurate. This would make the inversion more reliable and accurate, contributing to a better understanding of the anisotropy in the Bedretto Laboratory.

In summary, the study has given us important knowledge about the anisotropic behavior in the Rotondo granite. To deepen our understanding, it's crucial to address the aspects mentioned to achieve a more accurate and comprehensive characterization of anisotropy.

---

# Bibliography

- Bai, C.-Y., Huang, G.-J., Li, X.-L., Zhou, B., and Greenhalgh, S. (2013). Ray tracing of multiple transmitted/reflected/converted waves in 2-d/3-d layered anisotropic tti media and application to crosswell travelttime tomography. *Geophysical Journal International*, 195(2):1068–1087.
- Bauer, C., Hirschberg, S., Bauerle, Y., Biollaz, S., CalbryMuzyka, A., Cox, B., Heck, T., Lehnert, M., Meier, H., Prasser, H.-M., Schenler, W., Treyer, K., Vogel, F., Wieckert, C., Zhang, X., Zimmermann, M., Burg, V., Erni, M., Saar, M., and Tran, M. Q. (2017). Potentials, costs and environmental assessment of electricity generation technologies.
- Broker, K. and Ma, X. (2022). Estimating the least principal stress in a granitic rock mass: systematic mini-frac tests and elaborated pressure transient analysis. *Rock Mechanics and Rock Engineering*, 55(4):1931–1954.
- Cerveny, V. (2001). *Seismic ray theory*, volume 110. Cambridge university press Cambridge.
- Coskun, A., Bolatturk, A., and Kanoglu, M. (2014). Thermodynamic and economic analysis and optimization of power cycles for a medium temperature geothermal resource. *Energy conversion and management*, 78:39–49.
- David, C., Nejati, M., and Geremia, D. (2020). *On petrophysical and geomechanical properties of Bedretto Granite*. Laboratory report, ETH.
- Epiney, C. (2022). *Investigating anisotropic seismic velocities of the Rotondo granite in intact and fractured sections by crosshole seismic surveys*. Master’s thesis, ETH Zurich.
- Fa, L., Tang, J., Zhang, Q., Zhang, M., Zhang, Y., Liang, M., and Zhao, M. (2020). Reflection and refraction of elastic wave at vti-tti media interface. *Frontiers of Physics*, 15:1–17.
- Fichtner, A. (2021). *Lecture Notes on Inverse Theory*. Lecture notes, Department of Earth Sciences, ETH Zurich, Switzerland.
- Geotomographie (2011). *Manual for Borehole Geophone BGK series*. Manual, Geotomographie.

- Geotomographie (2015). *Manual for P-wave sparker SBS42 and S-wave source BIS-SH*. Manual, Geotomographie.
- Holmes, G. M., Crampin, S., and Young, R. (1993). Preliminary analysis of shear-wave splitting in granite at the underground research laboratory, manitoba. *Can. J. Expl. Geophys*, 29:140–152.
- Lützenkirchen, V. and Loew, S. (2011). Late alpine brittle faulting in the rotondo granite (switzerland): deformation mechanisms and fault evolution. *Swiss Journal of Geosciences*, 104:31–54.
- Ma, X., Hertrich, M., Amann, F., Bröker, K., Gholizadeh Doonechaly, N., Gischig, V., Hochreutener, R., Kästli, P., Krietsch, H., Marti, M., et al. (2021). Multi-disciplinary characterizations of the bedretto lab—a unique underground geoscience research facility. *Solid Earth Discussions*.
- Maurer, H. (2017). *Inverse Theory for Geophysics I: Basics*. Lecture notes, Institute of Geophysics, ETH Zürich.
- Rast, M., Galli, A., Ruh, J. B., Guillong, M., and Madonna, C. (2022). Geology along the bedretto tunnel: kinematic and geochronological constraints on the evolution of the gotthard massif (central alps). *Swiss Journal of Geosciences*, 115(1):8.
- Sayers, C. M. and Kachanov, M. (1995). Microcrack-induced elastic wave anisotropy of brittle rocks. *Journal of Geophysical Research: Solid Earth*, 100(B3):4149–4156.
- Sergeev, S. A., Meier, M., and Steiger, R. H. (1995). Improving the resolution of single-grain u/pb dating by use of zircon extracted from feldspar: Application to the variscan magmatic cycle in the central alps. *Earth and Planetary Science Letters*, 134(1-2):37–51.
- Shakas, A., Maurer, H., Giertzuch, P.-L., Hertrich, M., Giardini, D., Serbeto, F., and Meier, P. (2020). Permeability enhancement from a hydraulic stimulation imaged with ground penetrating radar. *Geophysical Research Letters*, 47(17).
- Thomsen, L. (1986). Weak elastic anisotropy. *Geophysics*, 51(10):1954–1966.
- Tsvankin, I. (2012). *Seismic signatures and analysis of reflection data in anisotropic media*. Society of Exploration Geophysicists.
- Yogeshwar, P. (2022). *Application of geophysical prospection methods in Earth and Environmental Sciences*. Lecture notes, Institute for Computational Geoscience and Reservoir Engineering, RWTH Aachen.

---

# Appendix A

---

## Appendix 1

### A-1 Crosshole seismic with S-wave sparker

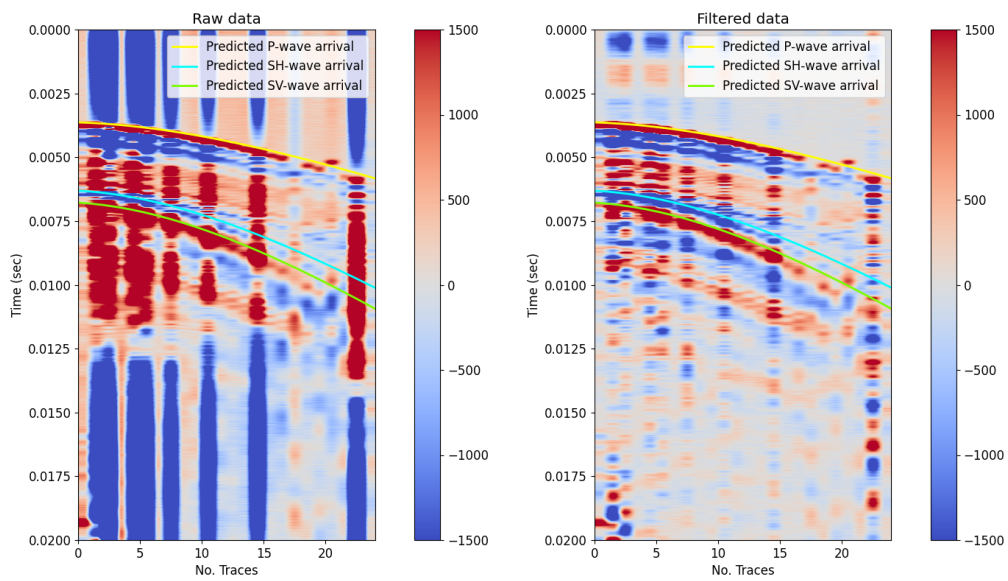


**Figure A-1:** Shot gather using S-waves sparker. Left: raw data. Right: filtered data with a highpass filter for 60 Hz.



Position 11



Position 12



Position 13



Position 13



Position 15



Position 16



Position 17

**Figure A-2:** Cable orientation at the top of the borehole for each rotation step.

## A-2 3-component geophone

### A-2-1 Hammering test

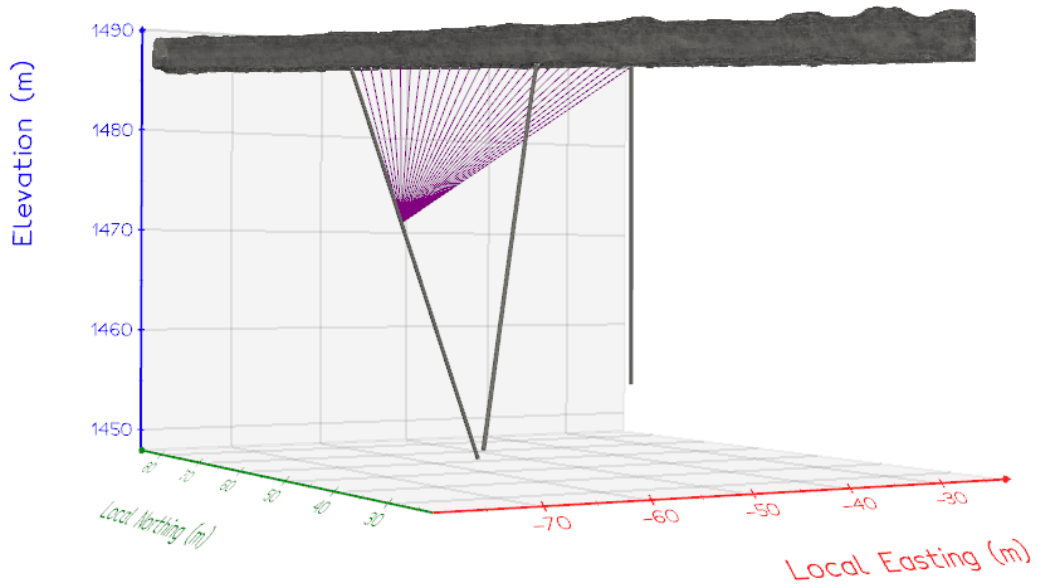


**Figure A-3:** Scheme of the rays for the survey conducted on April 27. The 3-component geophone was at SB2.3 and the tunnel floor was hammered with 1 m spacing.

### A-2-2 Crosshole seismic

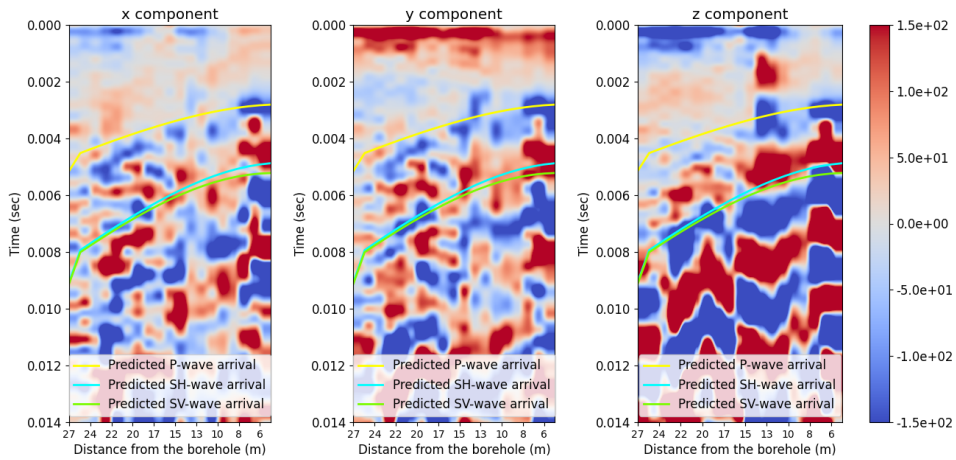


**Figure A-4:** Receiver gather when the 3-component geophone was placed in SB2.3 using a hammer as a source when the right side of the rail was being hammered.

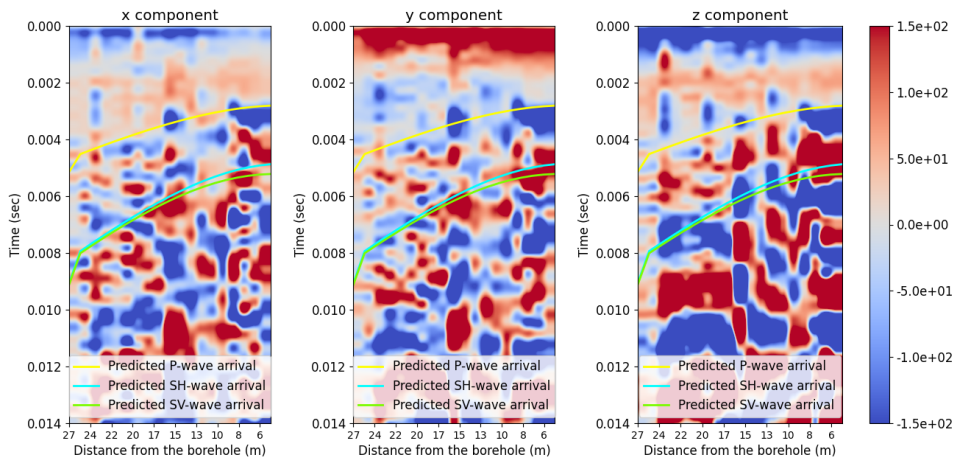


**Figure A-5:** Receiver gather when the 3-component geophone was placed in SB2.3 using a hammer as a source when the left side of the rail was being hammered.

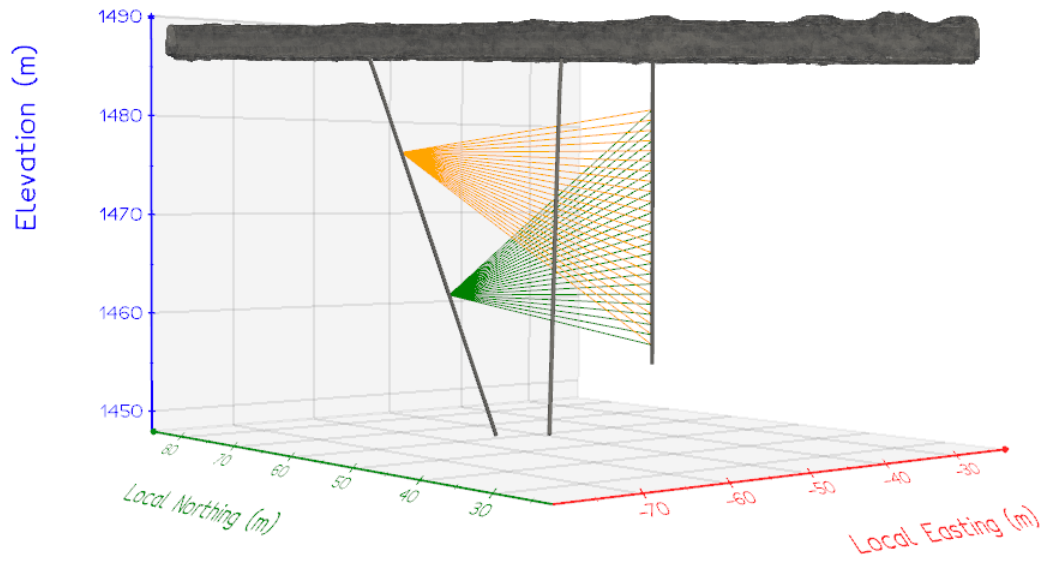


**Figure A-6:** Ray path representation for the cross-hole survey where the 3 component geophone was positioned at two different depths in SB2.3 and the source position was varied at SB2.1.

### A-2-3 Full 3-component geophone survey

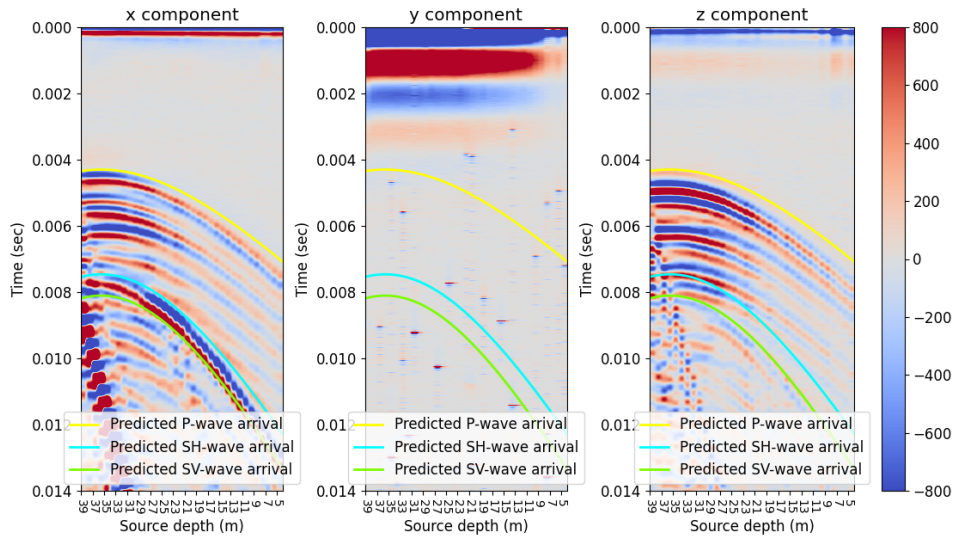


**Figure A-7:** Receiver gather after being rotated where the 3-component geophone was placed at 36 m depth in borehole SB2.2 and shots were made at SB2.3. It can be seen that no signal is recorded for the y-component of the geophone.